1-1-2011

Global properties of 'ordinary' early-type galaxies: photometry and spectroscopy of stars and globular clusters in NGC 4494

C. Foster
Swinburne University

L. R. Spitler
Swinburne University

Aaron J. Romanowsky
San Jose State University, aaron.romanowsky@sjsu.edu

D. A. Forbes
Swinburne University

V. Pota
Swinburne University

See next page for additional authors

Recommended Citation

C. Foster, L. R. Spitler, Aaron J. Romanowsky, D. A. Forbes, V. Pota, K. Bekki, J. Strader, R. N. Proctor, J. A. Arnold, and J. P. Brodie. "Global properties of 'ordinary' early-type galaxies: photometry and spectroscopy of stars and globular clusters in NGC 4494" *Monthly Notices of the Royal Astronomical Society* (2011): 3393-3416. https://doi.org/10.1111/j.1365-2966.2011.18965.x

Monthly Notices
of the
ROYAL ASTRONOMICAL SOCIETY

Mon. Not. R. Astron. Soc. **415,** 3393–3416 (2011) doi:10.1111/j.1365-2966.2011.18965.x

Global properties of 'ordinary' early-type galaxies: photometry and spectroscopy of stars and globular clusters in NGC 4494

Caroline Foster,[1⋆] Lee R. Spitler,[1] Aaron J. Romanowsky,[2] Duncan A. Forbes,[1] Vincenzo Pota,[1] Kenji Bekki,[3] Jay Strader,[4] Robert N. Proctor,[5] Jacob A. Arnold[2] and Jean P. Brodie[2]

[1] *Centre for Astrophysics & Supercomputing, Swinburne University, Hawthorn, VIC 3122, Australia*
[2] *UCO/Lick Observatory, University of California, Santa Cruz, CA 95064, USA*
[3] *School of Physics, University of New South Wales, Sydney, NSW 2052, Australia*
[4] *Harvard–Smithsonian Center for Astrophysics, 60 Garden Street, Cambridge, MA 02138, USA*
[5] *Universidade de São Paulo, IAG, Rua do Mato 1226, São Paulo 05508-900, Brazil*

Accepted 2011 April 21. Received 2011 April 18; in original form 2010 November 15

ABSTRACT

We present a comprehensive analysis of the spatial, kinematic and chemical properties of stars and globular clusters (GCs) in the 'ordinary' elliptical galaxy NGC 4494 using data from the Keck and Subaru telescopes. We derive galaxy surface brightness and colour profiles out to large galactocentric radii. We compare the latter to metallicities derived using the near-infrared Calcium Triplet. We obtain stellar kinematics out to ∼3.5 effective radii. The latter appear flattened or elongated beyond ∼1.8 effective radii in contrast to the relatively round photometric isophotes. In fact, NGC 4494 may be a flattened galaxy, possibly even an S0, seen at an inclination of ∼45°. We publish a catalogue of 431 GC candidates brighter than $i_0 = 24$ based on the photometry, of which 109 are confirmed spectroscopically and 54 have measured spectroscopic metallicities. We also report the discovery of three spectroscopically confirmed ultra-compact dwarfs around NGC 4494 with measured metallicities of $-0.4 \lesssim$ [Fe/H] $\lesssim -0.3$. Based on their properties, we conclude that they are simply bright GCs. The metal-poor GCs are found to be rotating with similar amplitude as the galaxy stars, while the metal-rich GCs show marginal rotation. We supplement our analysis with available literature data and results. Using model predictions of galaxy formation, and a suite of merger simulations, we find that many of the observational properties of NGC 4494 may be explained by formation in a relatively recent gas-rich major merger. Complete studies of individual galaxies incorporating a range of observational avenues and methods such as the one presented here will be an invaluable tool for constraining the fine details of galaxy formation models, especially at large galactocentric radii.

Key words: galaxies: abundances – galaxies: haloes – galaxies: individual: NGC 4494 – galaxies: kinematics and dynamics – galaxies: star clusters: general.

1 INTRODUCTION

Despite sustained efforts on both the observational and theoretical fronts, an accepted self-consistent picture of galaxy formation and evolution has not yet emerged. Key processes involved during galaxy formation and evolution include (but are not limited to) galaxy mergers, the accretion and/or dissipation of gas (whether early, via monolithic collapse, or merger induced), feedback processes such as stellar winds, supernova (SN) feedback or active galactic nuclei (AGN), reionization, etc.

Observational clues to the importance of these processes are crucial to our understanding of galaxy formation. For example, the relative importance of gas dissipation and energy feedback from stellar winds, SN and AGN as star formation quenching mechanisms needs to be constrained observationally. In principle, this can be studied through looking at radial abundance gradients in a galaxy (e.g. Bekki & Shioya 1999; Kobayashi & Arimoto 1999; Hopkins et al. 2009).

Also, the properties of progenitor galaxies involved in a merger can be probed by looking for distinct kinematic and morphological signatures in the merger remnant galaxy (e.g. Hopkins et al. 2009, 2010; López-Sanjuan et al. 2010), especially at large galactocentric

⋆E-mail: cfoster@astro.swin.edu.au

radii. Indeed, Hoffman et al. (2010) predict that the less relaxed intermediate and outer parts of a gas-rich (or wet) disc–disc merger remnant may retain the dynamical signature of the cold disc stars and original halo stars, respectively. In this model, a transition in the kinematic properties of the remnant is expected for $1 \lesssim r_e \lesssim 3$ where r_e is the effective radius. Moreover, as a complement to looking for these kinematic signatures, dry merging also leaves an imprint on the stellar populations of the remnant such that it washes out or weakens metallicity gradients (e.g. White 1980; Di Matteo et al. 2009; Pipino et al. 2010).

Thus, in order to obtain a complete picture and understanding of galaxy formation it is necessary to spectroscopically probe both the global kinematics and stellar populations present in galaxies out to large galactocentric radii (i.e. $>1\,r_e$). Unfortunately, the low surface brightness of galaxies in the outskirts hinders spectroscopic studies at large galactocentric radii. Spatially resolved kinematic and stellar population studies of the stellar light of large early-type galaxies (ETGs) are typically confined to the inner $\lesssim 1\,r_e$ (e.g. Reda et al. 2007; Emsellem et al. 2007, 2011; Kuntschner et al. 2010), thereby probing less than half the stellar light and potentially missing the important transition region previously discussed. To remedy this, Proctor et al. (2009, hereafter P09) have developed a technique that takes advantage of the large field of view of the DEep Imaging Multi-object Spectrograph (DEIMOS) spectrograph on Keck to extract galaxy light spectra from background spectra (sky + galaxy light) of the GC multi-slit observation and derive spatially resolved kinematics out to $3r_e$ (P09) and metallicities out to $\sim 1.5r_e$ (Foster et al. 2009, hereafter F09).

A good probe of early star formation are globular clusters (GCs). ETGs typically present a larger specific frequency (i.e. number per unit mass) of GCs than late-type galaxies (e.g. van den Bergh 1982; Ashman & Zepf 1992). GCs are generally measured to be old with ages comparable to the age of the Universe (e.g. Brodie et al. 2005; Strader et al. 2005; Puzia et al. 2005; Cenarro et al. 2007; Norris et al. 2008; Proctor et al. 2008) and thus probe the very earliest star formation episodes of their host galaxy. This known old age significantly diminishes the difficulties associated with the age–metallicity degeneracy (Worthey 1994) wherein old metal-poor populations share certain photometric and spectroscopic properties with those of young metal-rich populations. Moreover, GCs are well approximated as single-stellar populations (SSP), which greatly simplifies their stellar population analysis and interpretation.

Understanding the GC formation is crucial to understanding galaxy formation, especially the early epochs (West et al. 2004). For example, the nearly ubiquitous colour bimodality of the GC systems of most galaxies (see Brodie & Strader 2006, for a review) is usually interpreted as a metallicity bimodality with the blue and red GCs being metal-poor and metal-rich, respectively. This is a stringent constraint for galaxy formation scenarios that must provide at least two formation episodes or mechanisms to explain the colour bimodality (e.g. Lee et al. 2010; but see Muratov & Gnedin 2010).

A recent and extensive GC study is that of the kinematics and stellar populations of a statistically sizeable fraction of the GC system of the nearby giant ETG NGC 5128 by Woodley et al. (2010a,b). They find that the majority of the GCs in both subpopulations are old with a significant population of young metal-rich GCs forming later. They conclude that these young metal-rich GCs may have been formed in a more recent merging event than the bulk of the GCs. Moreover, both metal-rich and metal-poor GC subpopulations are found to be pressure supported with only mild rotation for the metal-rich GCs. From this, they are able to infer that the GC system of NGC 5128 is consistent with a hierarchical formation in a scenario similar to that proposed by Beasley et al. (2002) and Strader et al. (2005). This study demonstrates the power of combined spectroscopic and photometric studies of large samples of GCs to constrain the formation and assembly history of individual galaxies.

While the most massive nearby elliptical galaxies are in principle easier to study, their formation may have been atypical due to their often special location at the centre of large potential wells such as galaxy groups or clusters. Therefore, in order to obtain a complete view of galaxy formation, it is necessary to avoid 'special' environments and aim for more typical galaxy masses (i.e. $\sim M*$). To this end, we focus on the galaxy NGC 4494, which is often described as an 'ordinary elliptical' galaxy (e.g. Capaccioli, Caon & D'Onofrio 1992; Lackner & Ostriker 2010) mainly based on its typical light profile. Another aspect that makes it fairly ordinary, or average, includes its intermediate-density environment. Indeed, it has been described in the literature as either an isolated (Lackner & Ostriker 2010) or loose group member (Forbes et al. 1996; Larsen et al. 2001) as it is located at the edge of the Coma I cloud. It is neither a large nor a small galaxy with a stellar mass of $\sim 10^{11}$ $M_\odot$ (see Table 1). Its elliptical morphology is also typical as ETGs may contain over 50 per cent of the total stellar mass in the local Universe (Bell et al. 2003). It contains an inner dust ring ($r < 4$ arcsec, Lauer et al. 2005), is quite round with an axial ratio of $q = 0.87$ (see Table 1) and shows a very smooth luminosity profile with a central cusp (Lauer et al. 2007). Peculiarities include a kinematically decoupled core (Bender, Saglia & Gerhard 1994) or double maxima (Krajnovic et al. 2011) in the inner $\sim$19 arcsec beyond which sustained rotation ($V_{rot} \sim 60\,km\,s^{-1}$) is observed out to $\sim 3r_e$ with a possible 'pinching' or 'flattening' of the kinematics starting at $\sim 1.5r_e$ (P09). Other notable properties are a two order of magnitudes deficiency in X-ray luminosity for its optical luminosity (O'Sullivan & Ponman 2004) and a possible deficiency in dark matter (Romanowsky et al. 2003; Napolitano et al. 2009, hereafter N09).

Our approach is to study NGC 4494 in great detail to constrain the formation of 'ordinary' elliptical galaxies. To this end we study its structure, kinematics and stellar populations, as well as its GCs, using imaging and spectroscopy. We also include literature data. Our study is unique and one of the most complete studies of an individual 'ordinary' elliptical galaxy and its GC system to date. We present arguably the first large catalogue of GC recession velocities in an *ordinary* ETG.

This paper is divided as follows. Section 2 presents the photometric and spectroscopic data. The surface brightness/density profile, kinematics, colours and metallicity distribution of the stars and GCs are found in Section 3. These results and their implication for the key science questions described above are discussed in Section 4. Finally, we give a brief summary and our conclusions in Section 5.

2 DATA

2.1 Imaging acquisition and reduction

Subaru Suprime-Cam (Miyazaki et al. 2002) imaging of NGC 4494 is analysed to understand the GC system and light profiles of NGC 4494. We obtained a *g*-band observation of NGC 4494 during a Gemini time exchange program (GN-2008A-C-12) on the night of 2008 April 2. Two additional bands (*r* and *i* bands) were acquired on a later date, 2010 April 4, through the Keck time exchange. The total exposure times are 805, 365 and 540 s in the *g*, *r* and *i* bands,

Table 1. Properties of nine massive ETGs with significant GC kinematic samples from the literature. Hubble types (column 2) are as per NASA/IPAC Extragalactic Data base (NED). PAs and axis ratios (columns 3 and 4) are from the Two Micron All Sky Survey (2MASS; Skrutskie et al. 2006). Distances (column 5) are based on surface brightness fluctuations (Tonry et al. 2001) and include the distance moduli correction of Jensen et al. (2003). Effective radii (column 6) are taken from the Third Reference Catalogue of Bright Galaxies (RC3; de Vaucouleurs et al. 1991) for all galaxies except NGC 5128, which is from Dufour et al. (1979). *B*- and *K*-band absolute magnitudes (columns 7 and 8) are calculated from RC3 and 2MASS apparent magnitudes, respectively, and using the distances quoted in column 5. Stellar masses (column 9) are calculated from the *K*-band magnitude of column 8 assuming an M/L_K ratio corresponding to the V03 SSP of age 10 Gyr and solar metallicity. Systemic velocities (column 10) are from NED. Central velocity dispersions (column 11) are as per Paturel et al. (2003).

Galaxy	Hubble type	PA_{phot} ($\circ$)	q_{phot} (K band)	Distance (Mpc)	r_e (arcsec)	M_B (mag)	M_K (mag)	Stellar mass ($10^{11}M_\odot$)	V_{sys} (km s^{-1})	σ_0 (km s^{-1})
(1)	(2)	(3)	(4)	(5)	(6)	(7)	(8)	(9)	(10)	(11)
M49	E2	163	0.81	15.1 ± 0.7	104	-21.5 ± 0.16	-25.5 ± 0.1	3.1 ± 0.3	997 ± 7	294 ± 3
M60	E2	108	0.81	16 ± 1	69	-21.2 ± 0.2	-25.2 ± 0.2	2.4 ± 0.4	1117 ± 6	335 ± 4
M87	cD	152	0.86	15 ± 1	95	-21.3 ± 0.1	-25.1 ± 0.1	2.2 ± 0.2	1307 ± 7	335 ± 5
NGC 1399	E1	150	1.00	19 ± 1	80	-20.8 ± 0.3	-25.0 ± 0.2	2.0 ± 0.4	1425 ± 4	342 ± 6
NGC 1407	E0	60	0.95	27 ± 3	70	-21.4 ± 0.3	-25.4 ± 0.3	3.0 ± 0.9	1779 ± 9	272 ± 6
NGC 3379	E1	68	0.85	9.8 ± 0.5	35	-19.7 ± 0.1	-23.7 ± 0.1	0.59 ± 0.06	911 ± 2	209 ± 2
NGC 4494	E1-2	173	0.87	15.8 ± 0.9	49	-20.4 ± 0.2	-24.2 ± 0.2	1.0 ± 0.2	1344 ± 11	150 ± 4
NGC 4636	E0-1	143	0.84	13.6 ± 0.9	89	-20.2 ± 0.2	-24.2 ± 0.1	0.95 ± 0.08	938 ± 4	203 ± 4
NGC 5128	S0	43	0.89	3.9 ± 0.3	305	-20.2 ± 0.2	-24.0 ± 0.1	0.78 ± 0.07	547 ± 5	120 ± 7

respectively. The seeing conditions in the respective bands are: 0.63, 0.56 and 0.58 arcsec. Suprime-Cam data are prepared for analysis using standard imaging reduction techniques and a modified version of the SDFRED data pipeline (Yagi et al. 2002; Ouchi et al. 2004). The Suprime-Cam field of view covers a $\sim$36 $\times$ 29 arcmin region centred on NGC 4494.

Suprime-Cam photometry is bootstrapped to the Sloan Digital Sky Survey DR7 (Abazajian et al. 2009) photometric system using point sources with $19 \leq i \leq 21.5$ mag. The estimated *g*-, *r*- and *i*-band systematic uncertainty due to this calibration is 0.004, 0.005 and 0.004 mag, respectively. All photometry is Galactic extinction-corrected according to Schlegel, Finkbeiner & Davis (1998).

The images are prepared for the GC analysis by first modelling with IRAF/ELLIPSE and subtracting the galaxy light profiles. ELLIPSE is set to allow the centre, position angle (PA) and ellipticity to vary. A bright blue star is $\sim$6 arcmin away from NGC 4494 to the NNE. The scattered light from this star extends to a radius of $\sim$3.5 arcmin, thus IRAF/ELLIPSE is also used to model and subtract its light in the *g*, *r* and *i* bands. Because the star and galaxy profiles overlap significantly, ELLIPSE is performed and subtracted iteratively on the light profiles three times. The final image products show a constant background value across the field.

A catalogue of GC candidates is constructed from the three Suprime-Cam mosaics. At the distance of NGC 4494, GCs are unresolved and appear as point sources on the images. IRAF/DAOPHOT/FIND is used to locate objects on the field deviating by 3.8σ from a global background level. The difference between two different aperture magnitudes is used as a way to identify and remove extended sources from the GC catalogue (see e.g. Spitler et al. 2008). This is done for detected objects in each image. Aperture corrections are applied to the point sources and the photometric zero-points derived from the above procedure are used. The three separate photometry catalogues are combined using a matching threshold of 1 arcsec.

To supplement the Suprime-Cam catalogue, an existing *Hubble Space Telescope* (*HST*) Wide-field Planetary Camera 2 (WFPC2) GC catalogue is incorporated into the GC analysis. The WFPC2 catalogue is provided by S. Larsen and is described in Larsen et al. (2001). See Section 3.2.1 for details on our selection of GC candidates.

2.2 Spectroscopy acquisition and reduction

Spectra were obtained as part of the Spectroscopic Mapping of Early-Type Galaxies to Their Outer Limits (SMEAGOL) survey[1] on two separate dark nights: 2008 April 8 (hereafter Night 1) and 2009 March 23 (hereafter Night 2) using the DEIMOS on the Keck telescope. Three slit-masks were observed during Night 1 under good seeing conditions [full width at half-maximum (FWHM) $\sim$ 0.7 arcsec] and two slit-masks were observed during Night 2, this time under variable seeing conditions ($0.8 \lesssim$ FWHM $\lesssim 1.3$ arcsec). The galaxy light data only for Night 1 were presented in both P09 and F09. In addition to the data used in P09 and F09, the final data set used here includes roughly twice as many galaxy light spectra and the whole set of GC spectra. The 1200 lines mm^{-1} grating centred on 7800 Å was used together with 1 arcsec slitwidth. This setup yields a resolution of $\Delta\lambda \sim 1.5$ Å and allows for the coverage of the Calcium II Triplet (CaT) spectral region ($\sim$8400–8900 Å). A total of three and four half-hour exposures were taken yielding a total exposure time of 1.5 and 2 h per mask for Night 1 and 2, respectively. Fig. 1 shows the positions of the slits that returned useful science spectra.

The DEIMOS data are reduced using the IDL SPEC2D data reduction pipeline provided online. Flat-fielding using internal flats, wavelength calibration using ArKrNeXe arc lamps, as well as the local sky subtraction are performed within the pipeline. The pipeline outputs the GC spectra with their corresponding fully propagated variance arrays as well as the subtracted background or 'sky' spectra for each slit. Fig. 2 shows example GC spectra for a range of signal-to-noise ratios.

We use the Stellar Kinematics with Multiple Slits (SKiMS) technique described in P09 and F09 to extract the galaxy light spectra from these background spectra. Indeed, a background spectrum is essentially the sum of the pure sky and the galaxy light spectra. Therefore, if one has a good estimate of the sky's contribution to the background spectrum, it is possible to extract the galaxy light spectrum. For each mask, we obtain a high signal-to-noise ratio estimate of the 'pure' sky spectrum by summing and normalizing

[1] http://sages.ucolick.org/surveys.html

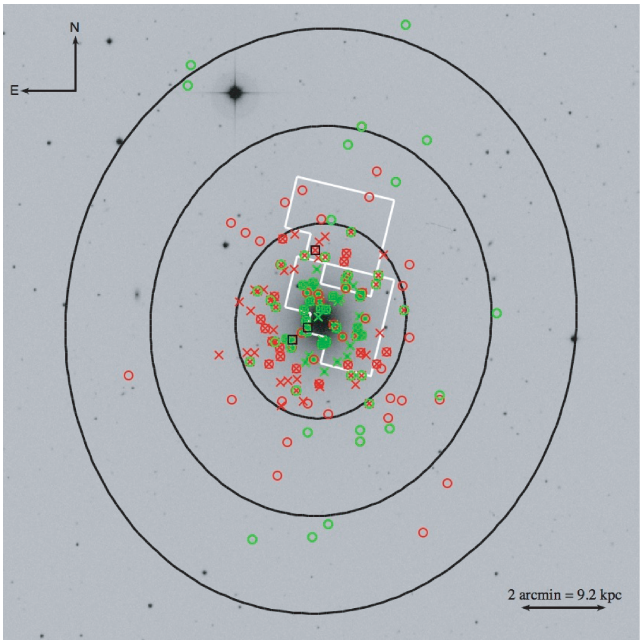

Figure 1. The DSS image of NGC 4494 showing the positions of our science spectra. Circles and squares represent kinematically confirmed GCs and UCDs, respectively, while crosses show the position of galaxy light spectra. Green and black small symbols are used when the spectrum returned both CaT and kinematic information, while red symbols are used if only kinematic information could be extracted. Large black ellipses represent 3, 6 and 9 r_e with the galaxy's global photometric PA and axial ratio. The *HST* field-of-view is shown in white. A colour version of this figure is available in the online version of this article.

several carefully selected background spectra at large radii (typically ∼6–7 r_e) where residual galaxy light is insignificant. This normalized sky spectrum is then scaled for each background spectrum using the sky scaling index defined in F09[2] as the excess flux in the central passband with respect to the continuum level. The central passband of the sky scaling index (8605.0–8695.5 Å) is measured between the blue (8478.0–8489.0 Å) and red (8813.0–8822.0 Å) continuum passbands. This scaled sky spectrum is subtracted from the background spectrum to obtain a galaxy light spectrum. As mentioned in F09, this method yields a final continuum level accurate to 0.7 per cent of the noise in the skyline residuals in the sky index definition region. The majority (∼90 per cent) of the amplitude of these skyline residuals are likely due to the intrinsic difficulties associated with non-local sky subtraction techniques such as variations of the sky spectrum across the DEIMOS field of view and with time. The additional ∼10 per cent of the amplitude of the skyline residuals in our science galaxy spectra are caused by small variations in the wavelength solution across the mask. Fig. 3 shows example galaxy light spectra for a range of signal-to-noise ratios.

3 ANALYSIS AND RESULTS

In this section we describe how we extract the photometric, kinematic and stellar population information for both the galaxy light and the GC system. We also give an overview of the method used to fit the kinematics of NGC 4494. These results are interpreted and discussed in Section 4.

[2] The sky scaling index was redefined in F09 in order to better avoid spectral features and differs slightly from that of P09 (see F09, for details).

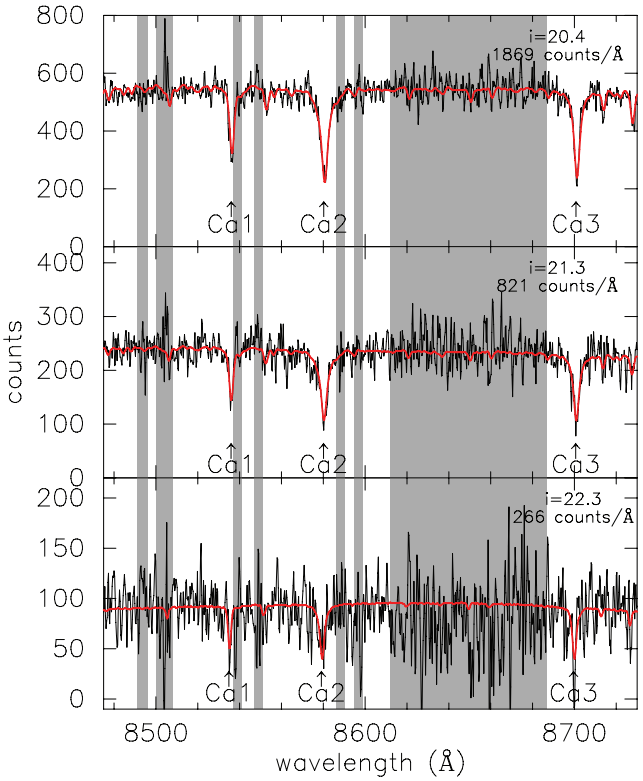

Figure 2. Example GC spectra (black) and fitted pPXF templates (red) for a bright (top panel), typical (middle panel) and faint (lower panel) GC in our sample. Shaded wavelength bands are regions affected by significant skyline residuals. GC apparent i_0 magnitudes are given.

3.1 Galaxy light

3.1.1 Stellar light profile

We first quantify the stellar light distribution of NGC 4494. Fig. 4 shows the surface brightness profile extracted as described in Section 2.1 in the *g* and *i* bands together with literature values. We fit Sérsic profiles (Sérsic 1963) to the surface brightness profile ($\mu(r)$) with geometric radius $r > 5$ arcsec to avoid the inner disc as per N09. In practice, we fit

$$\mu(r) = \mu_e + \frac{2.5b_n}{\ln(10)}\left[(r/r_e)^{1/n} - 1\right] \quad (1)$$

where $b_n = 1.9992n - 0.3271$ (i.e. equation 6 of Graham & Driver 2005) for the Sérsic index (n), the effective radius (r_e) and the surface brightness at the effective radius (μ_e). The resulting fits are shown in Fig. 4 and Table 2. We measure values between $48 \leq r_e \leq 55$ arcsec depending on the photometric filter used. Throughout this work we use the literature value of $r_e = 49$ arcsec ≈3.76 kpc (Table 1) as it lies within the range of our measured values and is thus a good compromise.

3.1.2 Stellar kinematics

The stellar kinematics of NGC 4494 have been probed out to large radii in P09 using the SKiMS method. Here, our galaxy spectral sample is roughly twice that of P09. We measure the velocity moments (recession velocity, velocity dispersion and Gauss–Hermite coefficients h_3 and h_4) for all the galaxy light spectra using the pPXF routine described in Cappellari & Emsellem (2004). The pPXF routine uses a set of 13 stellar templates to determine the best

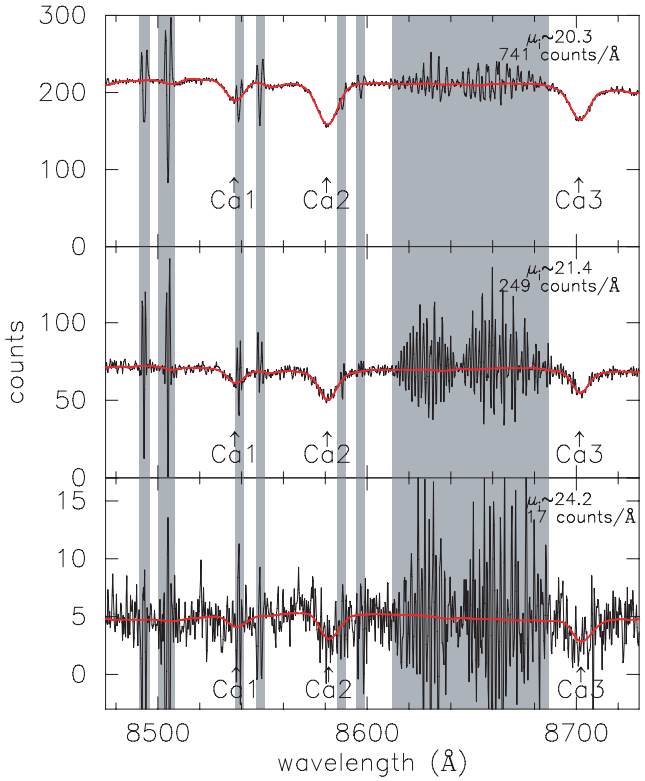

Figure 3. Example galaxy light spectra (black) and fitted pPXF templates (red) for a high (top panel), typical (middle panel) and low (lower panel) signal-to-noise ratio spectrum. Shaded wavelength bands are regions affected by significant skyline residuals. Galaxy i_0 surface brightness is given.

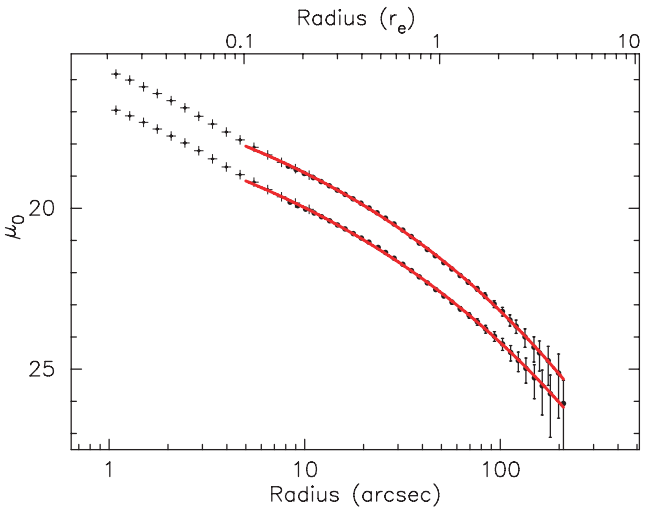

Figure 4. Surface brightness profiles for NGC 4494 as a function of intermediate radius (i.e. $\sqrt{ab}$ where a and b are the semimajor and semiminor axes, respectively). Filled circles are a compilation of our Subaru profiles and those from Lauer et al. (2005). Offsets were applied to the Lauer et al. (2005) V and I profiles to match our g and i profiles, respectively. Sérsic fits to the outer regions ($r > 5$ arcsec) are shown as red solid lines.

Table 2. Results of Sérsic fits to the galaxy surface brightness profile as a function of geometric radius (equation 1 fitted for μ_e, r_e and n) for points with $r > 5$ arcsec. Sérsic fits to the GC density profiles (equation 6 fitted for N_e, R_e, n and bg) are also listed.

Sample	$\mu_e \vert N_e$ (mag) $\vert$ (arcmin^{-2})	$r_e \vert R_e$ (arcsec)	n	bg (arcmin^{-2})
Galaxy g	22.81 ± 0.03	54.6 ± 0.8	3.72 ± 0.09	–
Galaxy r	21.90 ± 0.03	53.0 ± 0.6	3.52 ± 0.09	–
Galaxy i	21.51 ± 0.02	48.2 ± 0.5	3.47 ± 0.06	–
All GCs	5 ± 1	100 ± 10	1.7 ± 0.5	0.28 ± 0.02
Blue GCs	2.2 ± 0.8	138 ± 24	1.8 ± 0.7	0.22 ± 0.03
Red GCs	3.1 ± 0.4	83 ± 6	0.8 ± 0.2	0.053 ± 0.005

overall kinematic parameters and weighted combination of templates that minimizes the residuals between the spectrum and the final resulting fit (see Cappellari & Emsellem 2004, for more details). The templates were observed using DEIMOS on the nights of 2007 November 12–14 with a comparable instrumental setup. They cover a range of stellar sizes (11 giant and two dwarf stars) and span spectral types from F to early M, which dominate around this spectral region. The fitted spectral range is limited to 8450–8750 Å for stability and regions heavily contaminated by skylines are not fitted (see Fig. 3). Each fit is carefully inspected for quality control. Uncertainties on the measured velocity moments are estimated using Monte Carlo methods. For each spectrum, we randomly reshuffle the residuals between the best-fitting template and the original spectra in the wavelength region fitted by pPXF before re-fitting. This is repeated 100 times for each individual spectrum. We use the standard deviation on the velocity moments for the 100 Monte Carlo realizations as our estimate of the random uncertainty.

Fig. 5 shows the velocity moments as a function of PA for our sample of spectra. Individual values can be found in Table A1. The galaxy stars show clear major-axis rotation. The amplitude of the rotation is roughly constant all the way out to $>2r_e$ and shows a flattening (i.e. axial ratio $q_{kin} = 0.42 \pm 0.06$ is low) at large radii ($r \gtrsim 2r_e$). The velocity dispersion decreases with radius. For the inner h_3 measurements, we find a clear trend with PA although such a trend is not clearly visible beyond $1r_e$. The fourth velocity moment (h_4) has constant amplitude at all radii within the uncertainties.

In order to better understand the kinematic structure of NGC 4494, we use kinemetry to fit the model of an isotropic rotating ellipsoid (or inclined disc). Kinemetry is an analogue to photometry where instead of fitting a model of the stellar light distribution, we fit a model of the kinematics (see e.g. Krajnović et al. 2006, P09). In what follows, we generalize and improve on the technique presented in P09 to obtain kinemetry fits to discrete and semi-discrete two-dimensional data. P09 have shown that kinemetry using this model provides a good fit to the inner regions probed by SAURON (Emsellem et al. 2004). In contrast to P09 where the data were binned in *circular* annuli, here the data are binned in overlapping 'radial' (semimajor axis) intervals that, together with the PA and axial ratio, define *'elliptical annuli'*. The j^{th} annulus (or bin) contains a subset of N_j observed recession velocity data points ($V_{obs,i}$). We initially assume that the kinematic PA and axial ratio of the galaxy coincide with the photometric values. The PA and axial ratio of the j^{th} elliptical annulus are iteratively refined to match the kinematics as the algorithm fits for the kinematic position angle ($PA_{kin,j}$), axial ratio ($q_{kin,j}$) and the amplitude of the rotation ($V_{rot,j}$) using χ^2 minimization.

In practice, we first define an inner elliptical annulus ($j = 1$) whose short semimajor axis length (a_j) is the distance to the closest data point and whose long semimajor axis length is $a_j + \Delta a_j$. We perform a χ^2 minimization of the data points contained within this elliptical annulus to the model. For the j^{th} annulus, the χ^2 is

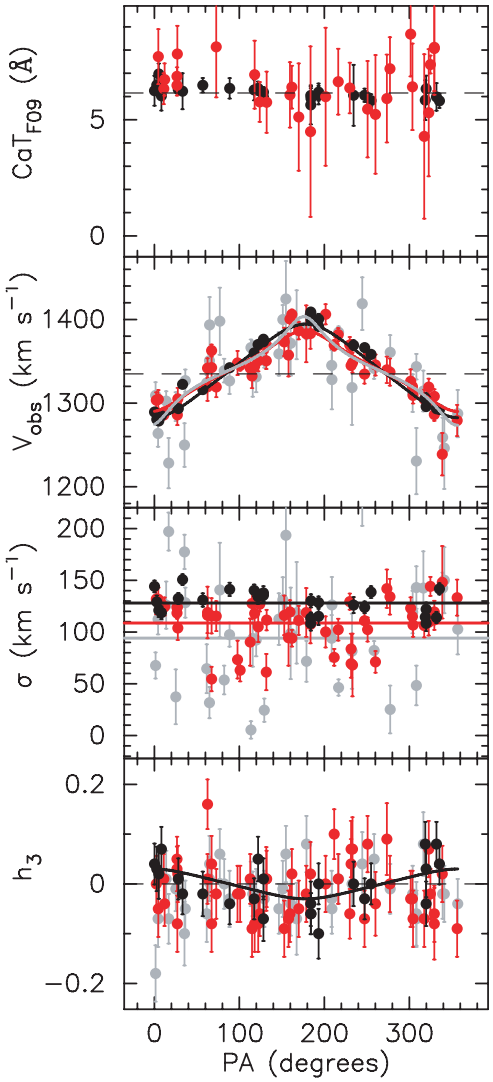

Figure 5. Variation in CaT_{F09} and velocity moments of the galaxy light as a function of PA for spectra with $r \leq 1r_e$ (black), $1r_e < r \leq 2r_e$ (red) and $r > 2r_e$ (grey). Kinemetry fits are shown with solid lines for the observed recession velocity (V_{obs}) and velocity dispersion in each radial bin, as well as for h_3 for spectra within $1r_e$. Dashed lines represent the CaT_{F09} saturation level (top panel), systemic velocity (second panel) and $h_3 = 0$ (bottom panel). The photometric PA is $PA_{phot} = 173°$. This figure is available in colour in the online version.

computed using the following equation:

$$\chi^2_{V,j} = \sum_{i=1}^{i=N_j} \frac{1}{(\Delta V'_{obs,i})^2} \left(V_{obs,i} - V_{mod,i,j}\right)^2, \quad (2)$$

where

$$V_{mod,i,j} = V_{sys} \pm \frac{V_{rot,j}}{\sqrt{1 + \left(\frac{\tan(PA_i - PA_{kin,j})}{q_{kin,j}}\right)^2}}, \quad (3)$$

and the ambivalent sign is positive (negative) if $(PA_i - PA_{kin,j})$ is in the first or fourth (second or third) quadrants. In equations (2) and (3), PA_i and $\Delta V'_{obs,i}$ are the position angle and the uncertainty on the recession velocity measurement of the i^{th} data point, respectively. The systemic velocity of NGC 4494 ($V_{sys} = 1338.5$km s^{-1}) is measured by fitting the inner, highest signal-to-noise ratio, data only prior to fitting the full data set.

For each iteration within the j^{th} annulus, a new set of parameters ($V_{rot,j}$, $PA_{kin,j}$, $q_{kin,j}$) is found and the values of $PA_{kin,j}$ and $q_{kin,j}$ are used to update the shape and orientation of the elliptical annulus to be used in the next iteration (a_j and Δa_j remaining fixed). Therefore, by construction this changes the selected member data points in the j^{th} bin slightly for each iteration. After 15 iterations, we move out to the next 'radial' bin [i.e. $(j + 1)$] by increasing the length of the short semimajor axis such that $a_{j+1} = a_j + (\Delta a)/3$. The factor of 1/3 used here is chosen to increase the number of radial sub-samples or bins in order to smoothly define the kinemetry radial profile. The semimajor axis binwidth (Δa_{j+1}) increases as a function of a_{j+1} according to a de Vaucouleurs (de Vaucouleurs 1953) surface brightness profile [i.e. $\propto 1/(a_{j+1})^{1/4}$] in order to compensate for the lower signal-to-noise ratio at large galactocentric distances. With this setup, there are 15 overlapping bins, each containing ∼25 data points. This process continues until the radial extent of the data is covered.

In order to obtain a χ^2/d.o.f. ≈ 1 at all radii and particularly in the inner regions we add an uncertainty of 5 km s^{-1} in quadrature to the Monte Carlo uncertainties [i.e. $\Delta V'_{obs,i} = \sqrt{(\Delta V_{obs,i})^2 + (5\,\mathrm{km\,s^{-1}})^2}$, see Table A1]. While the relative amplitudes of the uncertainties are crucial in order to obtain stable fits, this monotonic increase of the estimated uncertainties has a negligible effect on our fitted values. Nevertheless, it is an indication that either (1) there are velocity substructures at small galactocentric radii such that the model of a simple rotating isotropic ellipsoid is not appropriate or (2) the uncertainties are slightly underestimated. Indeed, the latter is likely since our quoted random uncertainties are obtained using Monte Carlo methods on our spectra and not independent measurements. For example, due to the finite (non-zero) length of the slits on the mask, their PA, the effects of seeing, etc., independent measurements of the kinematics for the same 'position' around the galaxy using either another instrument, setup or mask could yield slightly different values. For this reason, there could reasonably be some unaccounted for systematics of order ∼5 km s^{-1}. Finally, two data points deviating from the best fit at the $>3\sigma$ level were excluded.

The kinemetry fits for the higher order velocity moments (velocity dispersion and h_3) are done in parallel in each annulus and using the values of $PA_{kin,j}$ and $q_{kin,j}$ obtained from the recession velocity kinemetry fits. In principle the PA and axial ratio of these higher order velocity moments need not be equal to those of the recession velocity, but our data do not constrain these two parameters properly. Indeed, the velocity dispersion data in Fig. 6 show a hint of a dip along the minor axis (PA ∼ 83° and 263°) for points beyond $\sim 1r_e$ (i.e. red and grey points), suggesting that the kinematic flattening (i.e. low q_{kin}) is present in the velocity dispersion also. While this dip is suggestive, we are unable to reliably fit the axial ratio of the velocity dispersion explicitly with the current data set and assume that of the recession velocity moment.

In practice, for the j^{th} bin we fit the velocity dispersion (σ_j) using χ^2-minimization where

$$\chi^2_{\sigma,j} = \sum_{i=1}^{i=N_j} \left(\frac{\sigma_{obs,i} - \sigma_j}{\Delta\sigma'_{obs,i}}\right)^2. \quad (4)$$

Equation 4 is different in form from equation (2) because the velocity dispersion is an even moment. In equation (4), $\sigma_{obs,i}$ and $\Delta\sigma'_{obs,i} = \sqrt{\Delta\sigma^2_{obs,i} + (8\,\mathrm{km\,s^{-1}})^2}$ are the measured recession velocity of the i^{th} spectrum and its associated random uncertainty ($\Delta\sigma_{obs,i}$) with an additional uncertainty of 8 km s^{-1} added in

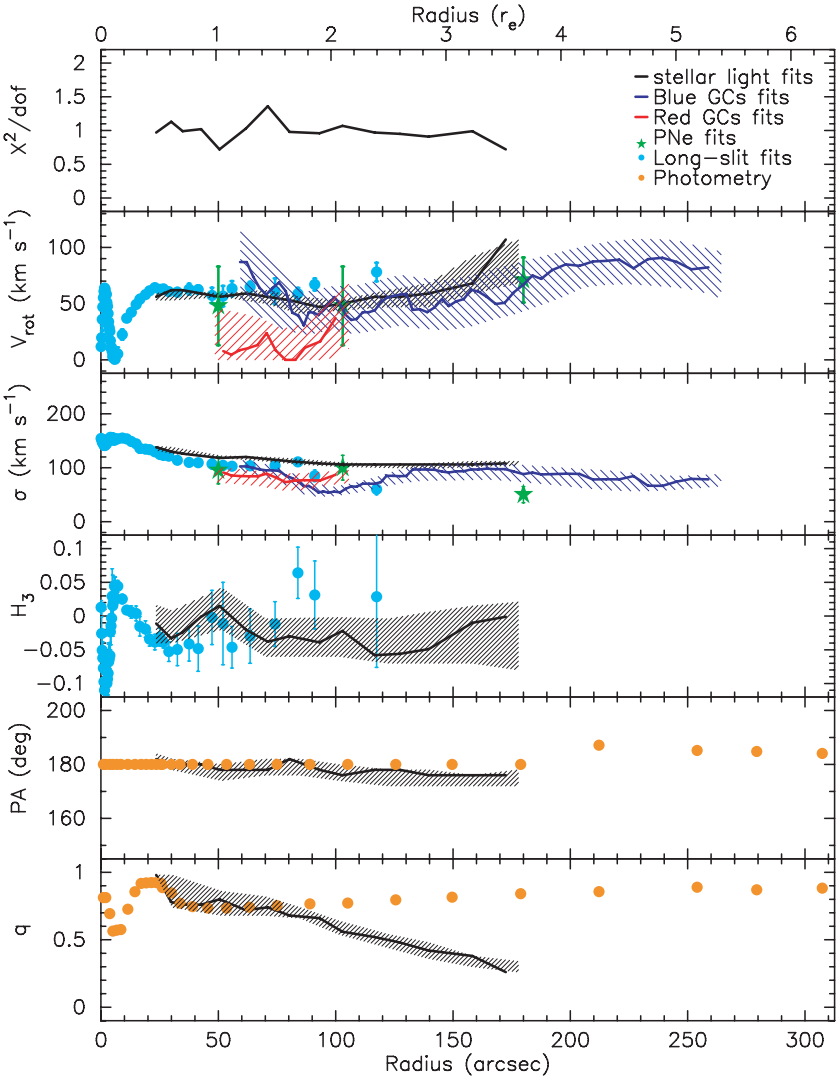

Figure 6. Results of our kinemetry fits (solid lines) as a function of the major axis equivalent radius ($1r_e = 49$ arcsec $\approx$3.76 kpc) with 68 per cent confidence intervals (hatched regions). Black, dark blue and red represent fits to the stellar light, the blue and red GCs, respectively. The top panel shows the value of the χ^2 per degree of freedom (d.o.f.) for the fits of the first velocity moment only (i.e. V_{rot}). Light blue, green and orange filled symbols show results of N09 and Coccato et al. (2009) from long-slit spectra, planetary nebulae (PNe) and galaxy light photometry, respectively. This figure is available in colour in the online version.

quadrature in order to obtain a χ^2/d.o.f. ≈ 1 as for the fits to V_{obs} above, respectively.

A similar approach is applied to fit the *amplitude* of the third (H_3) moment. Measurement uncertainties on individual velocity moments are propagated for the kinemetry fits using Monte Carlo methods. For each individual data point we have a measured uncertainty. Assuming that these uncertainties are Gaussian, we have a known distribution of possible measurements for each data point. Thus, for each point we randomly select from that distribution. Each time this is done for the entire data set and we get a new set of possible measurements. The kinemetry algorithm described above is then applied to the new data set. This exercise is repeated 100 times. From the resulting range of fits we determine the 68 per cent confidence interval of the best fit model allowed by the data.

We also use Monte Carlo methods to verify that kinemetry can be reliably applied to sparse data. We create a series of rotating ellipsoid models by varying the input rotational velocity $V_{rot,in} =$ 50, 80 and 100 km s^{-1}, and kinematic axial ratio $q_{kin,in} = 0.5$, 0.8 and 1.0. For each model, we randomly sample 115 data points within $\sim 3r_e$ and assign measurement errors consistent with our observed errors at that radius. This is repeated 25 times for each of the ($V_{rot,in}$, $q_{kin,in}$) combinations. We verify how well the input parameters are then recovered using kinemetry. In general, we find that the standard deviation of the output rotational velocity varies between $\sigma_{V_{rot,out}} = 5$ and 7 km s^{-1}, while $\sigma_{q_{kin,out}} \sim 0.1$ for all $q_{kin,in}$. We find that the fits are less stable when both $V_{rot,in}$ and $q_{kin,in}$ are low. We do not find other 'unexpected' systematics. We conclude that kinemetry can be applied to sparse data successfully provided that there is sufficient rotation.

The results of the kinemetry fits to the data are shown in Fig. 6. In general, we find good agreement between the long-slit and PNe results of N09 and Coccato et al. (2009) and our data from the SKiMS method. We have also tried fitting the PNe data from N09 using our method for discrete velocities (see Section 3.2.3) and find good general agreement with Coccato et al. (2009) except around $2r_e \lesssim r \lesssim 3r_e$ where the fits did not converge due to an

apparently low rotation. The trends described above and found by P09 are confirmed. We find sustained major-axis rotation at all radii consistent with both the results of N09 and Coccato et al. (2009). We do not find evidence for minor-axis rotation. There is a slight decrease in velocity dispersion that levels off with radius at a value of $\sim$100 km s^{-1} beyond $\sim 2.3 r_e$ slightly at odds with the velocity dispersion estimated from PNe but consistent with that of the GCs (see Section 3.2.3). The amplitude of the third velocity moment levels off beyond $\sim 1.8 r_e$ at a value of $H_3 \sim -0.03$.

Emsellem et al. (2007) classified ETGs as slow- or fast-rotators according to a luminosity- and radius-weighted value of the angular momentum proxy $\lambda_R = V_{\rm rot}(r)/\ \overline{V_{\rm rot}(r)^2 + \sigma(r)^2}$, where slow- and fast-rotators correspond to $\lambda_R < 0.1$ and 0.1, respectively. These classifications were made for radii $\leq 1 r_e$, but P09 demonstrated that the picture could change dramatically with more radially extended data. In the case of NGC 4494, we find that a local $\lambda_R \sim 0.35$ (i.e. fast rotation) at virtually all probed radii, modulo a sharp dip around $0.1 r_e$ due to the kinematically decoupled core. In Emsellem et al. (2011), NGC 4494 is also found to be a fast-rotator using a new classification method that takes into account the ellipticity of the isophotes.

Although not as pronounced as originally found in P09, a slight kinematic twist is visible beyond $\sim 2 r_e$ such that the kinematic PA is different from the photometric PA at large radii. We measure a radial change in the axial ratio such that the velocity distribution becomes flattened (i.e. small $q_{\rm kin}$) as originally detected by P09. This behaviour is at odds with the measured isophotes that remain much rounder even at large radii with no sign of significant disciness. We test the robustness of the flattening of $q_{\rm kin}$ at large radii using three methods. The first is the above described nominal method in which we allow $q_{{\rm kin},j}$ to freely vary and iteratively define the bins accordingly. Secondly, similarly to the binning method used in P09, we let the fitted $q_{{\rm kin},j}$ vary but fix the bin shapes to $q_{\rm phot}$, i.e. we do not let the kinematic axial ratio define the axial ratio of the bins. While this yields an overall larger χ^2/d.o.f. value, lower values of $q_{{\rm kin},j}$ are still marginally preferred at large radii. Thirdly, we fix $q_{{\rm kin},j} = q_{\rm phot}$ for both the binning and the fitting and for all bins (j). This yields substantially larger χ^2/d.o.f. values than in the (first) nominal case. We conclude that the flattening of the kinematics is most robustly detected in the first method but is still marginally detected when the kinematic axial ratio is allowed to vary inside selection bins whose shape has fixed axis ratios. On the basis that the only self-consistent methods are the first and the third and given that the third method yields significantly higher χ^2/d.o.f. values than the first, we conclude that the former is preferable. We also tried removing the apparent 'outliers' located around PA $\sim 0^\circ$ and 360° with recession velocities below 1570 km s^{-1} to see if they were causing the flattening and the results did not change significantly. We conclude that the kinematic flattening is robust (i.e. $q_{\rm kin}$ is indeed low).

Fig. 7 shows the relationship between measured h_3 and $(V_{\rm obs} - V_{\rm sys})/\sigma$, which is a measure of the fraction of rotational over pressure support. The anti-correlation between h_3 and $(V_{\rm obs} - V_{\rm sys})/\sigma$ is indicative of a disc kinematic structure. This may be the source of the flattened kinematics.

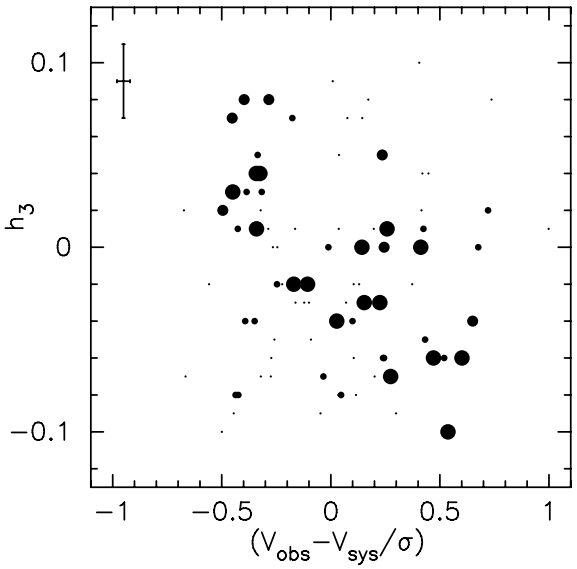

Figure 7. Relationship between the higher order Gauss–Hermite moments h_3 and $(V_{\rm obs} - V_{\rm sys})/\sigma$. Point sizes are proportional to the signal-to-noise ratio of the spectra. The anti-correlation between h_3 and $(V_{\rm obs} - V_{\rm sys})/\sigma$ suggests a disc structure is present. Typical error bars shown in the upper-left corner.

3.1.3 Stellar colours and metallicities

We investigate the radial colour gradient of the stars in NGC 4494. By doing this, we obtain a *rough* estimate of the radial metallicity gradient by assuming a fixed old GC-like age at all radii. In other words, we attribute any colour variation to changes in the metallicity (i.e. ignoring age effects). We convert $(g - i)_0$ colours into approximate metallicity using the empirical linear relationship derived by Sinnott et al. (2010) for GCs in NGC 5128. This is shown in Fig. 8. The galaxy stellar light is generally red and shows an overall colour/metallicity gradient. Because all the visible dust is contained within the inner 4 arcsec (Lauer et al. 2005), we will assume that dust is not affecting our inferences on the metallicity at the radii probed here. Therefore, between 10 and 70 arcsec (or $\sim 0.2 r_e < r < 1.4 r_e$), the colour profile suggests a moderate metallicity variation with radius of -0.17 ± 0.02 dex per dex. Assuming a younger age would increase the colour-inferred metallicity. Beyond $2 r_e$ the photometric uncertainties start to dominate.

We use the CaT as a spectroscopic proxy of metallicity. The CaT has been employed as a metallicity indicator for resolved red giant stars (e.g. Diaz, Terlevich & Terlevich 1989; Jorgensen, Carlsson & Johnson 1992; Koch et al. 2006), integrated light spectra of Galactic (e.g. Bica & Alloin 1987; Armandroff & Zinn 1988) and extragalactic (Foster et al. 2010, hereafter F10) GCs as well as galaxies (e.g. Cenarro, Cardiel & Gorgas 2008, F09). We compute the CaT index value for each galaxy spectrum using the index definition from F09 (i.e. $\rm CaT_{F09}$). The $\rm CaT_{F09}$ is corrected for velocity dispersion broadening and converted into [Fe/H] using the SSP models of Vazdekis et al. (2003, hereafter V03) following F09. Once again, we emphasize that the inferred galaxy starlight metallicities are uncertain due to the above caveats. Fig. 8 shows the CaT index as a function of the semimajor axis equivalent radius (as per equations 3 and 4 of F09). The $\rm CaT_{F09}$ gradient is found to be essentially flat at all probed radii indicating an undetectably small radial change in metallicity.

The V03 SSP models predict that the CaT features saturate at a metallicity of roughly [Fe/H] ≈ -0.5 such that there is a maximum allowed $\rm CaT_{F09}$ value of 6.18 Å.[3] This theoretical behaviour has

[3] This is different from the saturation value for $\rm CaT_{F10}$ because $\rm CaT_{F09}$ is an altogether different index. Therefore, the absolute values of the two CaT indices used in this work for GC and galaxy light spectra cannot be directly compared.

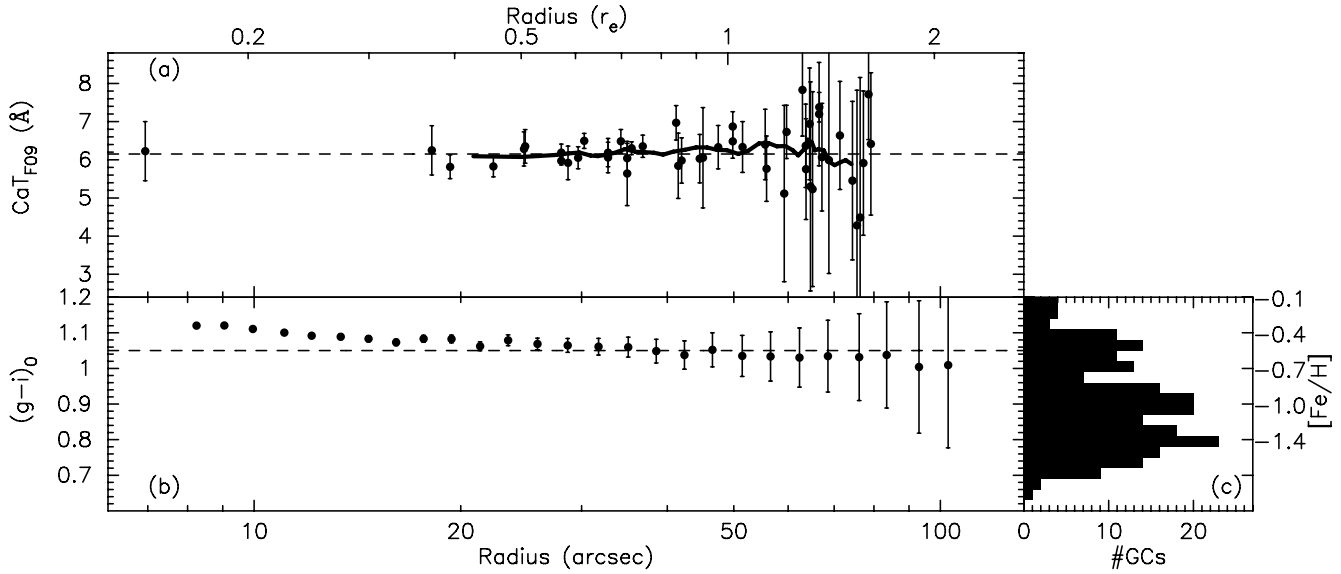

Figure 8. Panels (a) and (b) show the CaT_{F09} index and $(g - i)_0$ colour gradients of the NGC 4494 stellar light, respectively. Thin dashed lines show the saturation limit predicted by the V03 SSP models (i.e. $CaT_{F09} = 6.18$ Å or [Fe/H] ~ -0.5 dex). The thick solid line in Panel (a) is a rolling average (see e.g. Sawilowsky 2007) using bins of eight data points. Panel (c) is a colour histogram of the photometric sample of GCs with $i_0 < 23.5$ and $(g - i)$ conversion to metallicity as per Sinnott et al. (2010).

not been confirmed observationally. Our galaxy CaT_{F09} data are consistent with a saturation around 6.18 Å. Because our data scatter about this limit we cannot confidently use the V03 models to convert our CaT_{F09} values into metallicity. It is possible, however, that, as the colours suggest, the metallicity variation in the radial range probed is small (only Δ[Fe/H] $\sim$ 0.2 dex) and thus a variation in CaT_{F09} may be hard to detect within the uncertainties. Indeed, between 20 and 80 arcsec, where the vast majority of our CaT data lie, both the colours and CaT_{F09} values are consistent with the predicted saturation limit.

3.2 Globular cluster system

3.2.1 GC colours and candidate selection

As described in Section 2.1, we have a combination of both *HST*/WFPC2 and Subaru/Suprime-Cam imaging available. Various selections are applied to identified point sources in order to avoid contamination by foreground stars and background galaxies. We first apply an upper size cut in both the *HST* and the Subaru images[4] in order to remove clearly extended objects such as background galaxies. We also apply a spatial cut removing all objects beyond 8 arcmin ($\sim 10 r_e$) from the galactic centre to avoid further contamination that dominates beyond that radius (see Section 3.2.2). Our colour selections are as follows: (1) whenever *HST* imaging is available, GC candidates are selected based on $(V - I)_0$ colours only. (2) If *HST* imaging is not available, the selection is based on a colour–colour cut in $(r - i)_0$ versus $(g - r)_0$ space from the Subaru photometry (see Fig. 9). The final master GC catalogue of Subaru and *HST* photometry includes 431 selected GC candidates brighter than $i_0 = 24$. This catalogue is available online (also see Table 3).

Selecting bright objects in common between the *HST* and Subaru images beyond a galactocentric radius of 0.5 arcmin to avoid Subaru image artefacts, we obtain the following colour conversion:

$$(g - i)_0 = 1.23 \times (V - I)_0 - 0.25 \quad (5)$$

with an rms = 0.035 using a linear bisector fit (Feigelson & Babu 1992). We use this conversion to convert *HST* $(V - I)_0$ colours into $(g - i)_0$ to merge with the Subaru photometry.

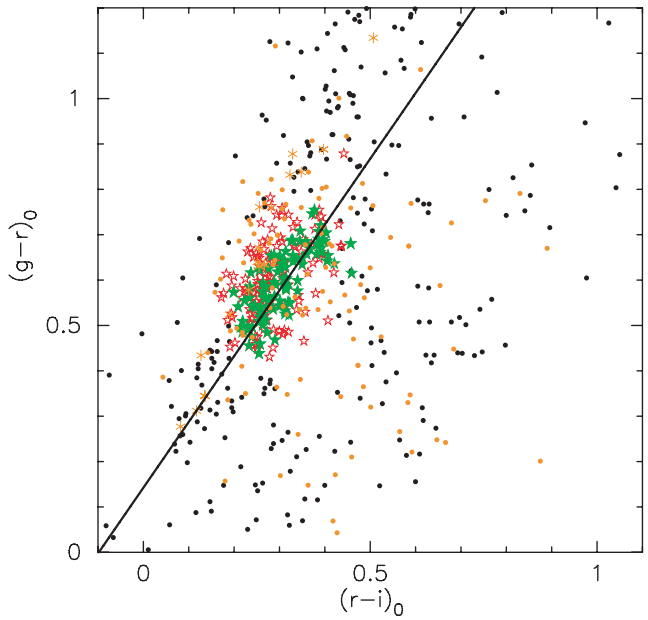

Figure 9. Visual representation of our applied colour–colour selection for objects with galactocentric radii <8 arcmin brighter than $i_0 = 23.5$. Filled green star symbols are spectroscopically confirmed GCs while hollow red stars show our photometrically selected GC candidates. The solid line is the inferred GC sequence [i.e. $(g - r)_0 = 1.450(r - i)_0 + 0.142$]. Spectroscopically confirmed stars (orange asterisk) and emission line galaxies (orange filled circles) observed either as contaminants or fillers are shown. This figure is available in colour in the online version.

[4] The size cut based on Subaru is only applied to objects beyond galactocentric radii of 0.5 arcmin because of crowding issues.

Table 3. Catalogue of photometrically selected GC candidates with $i_0 < 24$. Columns 1 and 2 give the position in right ascension and declination (J2000), respectively. Columns 3 to 7 are the Subaru/Suprime-Cam and *HST*/WFPC2 photometry. The full table is available in the online version – see Supporting Information.

α (hh:mm:ss) (1)	δ (hh:mm:ss) (2)	g_0 (mag) (3)	r_0 (mag) (4)	i_0 (mag) (5)	V_0 (mag) (6)	I_0 (mag) (7)
12:31:23.70	25:40:12.90	24.072 ± 0.023	23.359 ± 0.020	22.981 ± 0.019	–	–
12:31:07.44	25:40:15.96	24.362 ± 0.026	23.672 ± 0.022	23.319 ± 0.021	–	–
12:31:38.83	25:40:17.01	24.922 ± 0.032	24.271 ± 0.030	23.830 ± 0.028	–	–
12:31:08.79	25:40:27.99	23.805 ± 0.022	23.237 ± 0.018	22.991 ± 0.020	–	–
12:31:18.50	25:40:29.10	23.377 ± 0.020	22.823 ± 0.016	22.562 ± 0.018	–	–
12:31:36.43	25:40:34.57	22.326 ± 0.019	21.864 ± 0.015	21.662 ± 0.016	–	–
...	...	...	...	...	...	...

The final colour magnitude diagram (CMD) for all our GC candidates with $i_0 < 24$ is shown in Fig. 10. Three bright objects ($i_0 < 19.4$ mag) have recession velocities consistent with that of NGC 4494 but their absolute luminosity ($M_i < -10.9$ mag) suggests they fit within the definition of ultra-compact dwarfs (UCDs), or equivalently, dwarf-globular transition objects (DGTOs; see Section 3.2.5). All three UCDs are centrally located (within 2 arcmin or $\sim 4 r_e$ of NGC 4494's centre). Other bright objects ($i_0 <$ 19.4 mag) with colours consistent with the NGC 4494 GCs are uniformly distributed across the Subaru/Suprime-Cam field of view

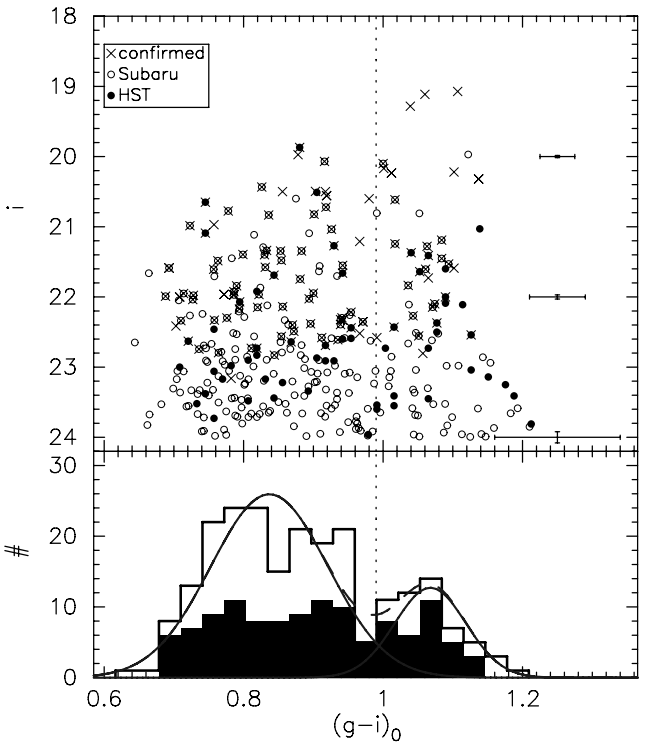

Figure 10. CMDs (top panel) for our GC candidates beyond 0.5 arcmin from the galactic centre selected based on Subaru (hollow circles) and *HST* (filled circles) imaging. All spectroscopically confirmed GCs around NGC 4494 are shown as crosses. Typical Subaru error bars are shown on the right-hand side of the top panel. Lower panel shows histograms for our candidates brighter than $i_0 = 23.5$ (hollow) with KMM fits for each/the sum of the two subpopulations as solid/dashed grey line(s) and confirmed (filled histogram) GCs. The colour distribution of the confirmed GCs is representative of that of the candidates. The dotted line represents our fiducial colour split.

(19×15 arcmin) suggesting that they are likely contaminant foreground stars. For this reason we apply a bright magnitude cut at $i_0 = 19.4$.

We check for the usual colour bimodality within our GC candidates in the combined *HST* and Subaru $(g-i)_0$ colour distributions. We apply the KMM (Ashman, Bird & Zepf 1994) test for the heteroscedastic (unequal widths) case to our GC candidates with $i_0 <$ 23.5. The colour histogram and fit results are shown in Fig. 10. The returned p-value is <0.0001, suggesting that a bimodal colour distribution is strongly favoured over a unimodal one at the >99.99 per cent level. The peaks for the blue and red GCs are at $(g-i)_0 = 0.84$ and 1.07, with widths of $\sigma = 0.084$ and 0.051, respectively. For comparison, Larsen et al. (2001) find peaks at $(V-I)_0 = 0.90$ and 1.10, corresponding to $(g-i)_0 = 0.86$ and 1.10, for the blue and red subpopulations when using the homoscedastic test on the *HST* data only. These small discrepancies are likely due to the intrinsic differences between the data sets (*HST* versus Subaru), possible intrinsic radial colour gradients (e.g. Harris 2009) and methods (homoscedastic versus heteroscedastic). Larsen et al. (2001) also infer a relatively equal number of GCs in each subpopulation. We choose to apply a nominal colour split at $(g-i)_0 = 0.99$, corresponding to $(V-I)_0 \sim 1.01$ based on the KMM results in order to separate the blue and red GCs. Using the Sinnott et al. (2010) conversion from $(g-i)_0$–colour to metallicity suggests that our colour split corresponds to a metallicity of [Fe/H] ~ -0.68 dex.

3.2.2 GC spatial distribution

We construct projected surface density profiles of the NGC 4494 GC system candidates. Independent photometric selection criteria (as described in Section 3.2.1) are applied to both the *HST* and Subaru data sets to generate GC catalogues for this analysis. Between 1 and 4 arcmin, there are reliable surface density data for both Subaru and *HST* GC catalogues. Within the uncertainties the Subaru profile agrees with the *HST* profile, as shown in Fig. 11.

We fit the GC density profile ($N(r)$) with a Sérsic profile (Sérsic 1963) similar to that commonly done for galaxy surface density profiles and recently extended to GC systems (Peng et al. 2011). We fit the following variation of equation (1) from Graham & Driver (2005):

$$N(r) = N_e \exp\left(-b_n\left[(r/R_e)^{1/n} - 1\right)\right] + bg, \quad (6)$$

where $b_n = 1.9992n - 0.3271$. Free parameters recovered are the Sérsic index (n) of the GC system, which is a measure of the steepness of the profile, the effective radius of the GC system (R_e), which gives us a measure of the extent of the GC system, the surface

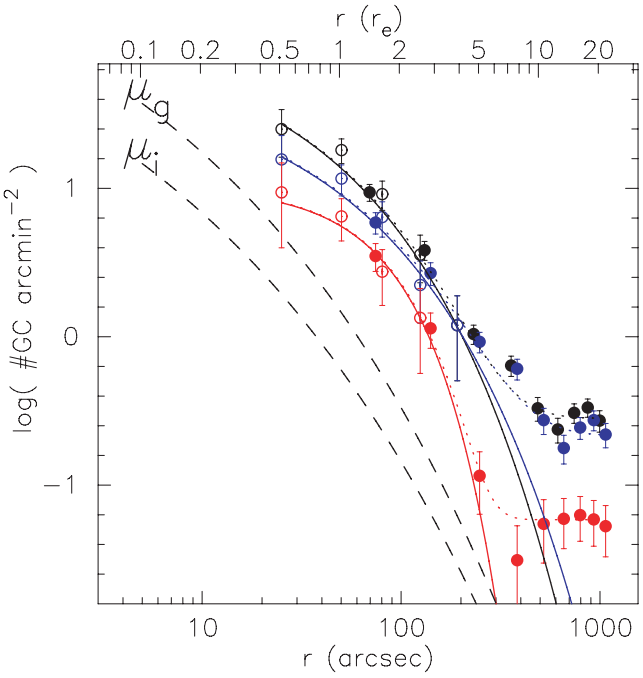

Figure 11. Surface density profiles of the NGC 4494 GC system. All, red and blue subpopulations are shown in black, red and blue, respectively. Open and filled symbols show the *HST* and Subaru data, respectively. Sérsic fits with and without background/contamination constant (see text) are shown as dotted and solid lines, respectively. Also shown are scaled and offset Sérsic profile fits to the galaxy surface brightness profiles in the g and i bands (μ) as labelled (see Section 3.1.1 and Fig. 4). This figure is available in colour in the online version.

density at that radius (N_e) and the background or contamination level (bg). The results of the fits are shown in Fig. 11 and Table 2. For comparison with previous studies, we also fit a Power-law profile [i.e. $N(r) \propto r^{\alpha}$]. We obtain slopes of $\alpha = -1.7 \pm 0.2$, -1.8 ± 0.2 and -2.2 ± 0.3 for all, blue and red GCs, respectively. As with other galaxies (e.g. Forbes et al. 1998; Dirsch et al. 2003; Bassino, Richtler & Dirsch 2006), the red GCs are more centrally concentrated than the blue GCs. This is also inferred from their respective effective radii ($R_{e,blue} = 138$ arcsec and $R_{e,red} = 83$ arcsec).

We use 500 Monte Carlo realizations to estimate the total number of GCs based on the best-fitting Sérsic parameters and their covariance matrix by separately integrating the density profiles for all, the blue and the red GCs to infinity. We also explicitly account for completeness and contamination. This yields an estimated number of GCs of 392 ± 49, 324 ± 74 and 125 ± 10 for all, red and blue GCs, respectively. Therefore, assuming $m_V = 9.70$ (RC3) as total galaxy magnitude and using other variables as per Table 1, the specific GC frequency S_N (Harris & van den Bergh 1981) is 1.2 ± 0.3, while T_N (Zepf & Ashman 1993) is 4 ± 1. This is somewhat low for galaxies of similar stellar mass but still within the observed range (see Spitler et al. 2008; Peng et al. 2008).

It has recently been shown that the correlation between total number of GCs and the central black hole mass (Spitler & Forbes 2009) is tighter than other previously observed correlations with black hole mass (see Burkert & Tremaine 2010; Harris & Harris 2011; Snyder, Hopkins & Hernquist 2011). Therefore, using equation (3) of Harris & Harris (2011), we estimate that the mass of the central black hole in NGC 4494 is $(1.6 \pm 0.2) \times 10^8\,M_{\odot}$.

3.2.3 GC kinematics

For the candidate GCs that have available spectra with sufficient signal-to-noise ratio, we first measure their recession velocity. We use the IRAF task RV.FXCOR to cross-correlate the spectra with the 13 stellar templates described in Section 3.1.2. Thus, for each GC we have 13 measured recession velocities together with output uncertainties from the FXCOR routine. The recession velocities reported in Table A2 are the average measured recession velocities using all 13 template cross-correlation results. The quoted uncertainties for the GC recession velocities are the maximum between 5 km s^{-1} or the average output uncertainties given by FXCOR, which correspond to the average width of the cross-correlation peaks, added in quadrature to the standard deviation among the templates, which is an estimate of the systematics. Some of our spectra cover sufficiently blue wavelengths to use the Hα feature at 6563 Å to confirm the measured recession velocity. Some of our spectra were from Galactic stars and background emission line galaxies. Table 4 shows the position of those contaminants and their recession velocity.

The spatial distribution of kinematically confirmed GCs is shown in Fig. 1. We look for rotation in the GC system around NGC 4494. We extend the kinemetry method described in Section 3.1.2 to discrete velocities and perform rolling or moving radial fits for the amplitude of the rotation (V_{rot}), the velocity dispersion (σ) and the kinematic position angle (PA_{kin}) simultaneously. Rolling fits are similar in principle to rolling or moving averages (Sawilowsky 2007) and were also used in P09 (see also Kissler-Patig & Gebhardt 1998, who use a very similar method). They are performed by first using the inner N_{bin} GCs to fit the kinemetry, then removing the innermost point and adding the next further point to refit the kinemetry, and so on, until all GCs have been exhausted. We use bins of 25 and 20 for the blue and red GCs, respectively. Gaussian line-of-sight velocity distributions are assumed. In practice, for the j^{th} radial bin we minimize the likelihood ratio (Λ_j):

$$\Lambda_j \propto \prod_{i=1}^{i=N_j} \left[\frac{(V_{obs,i} - V_{mod,i,j})^2}{(\sigma_j^2 + (\Delta V_{obs,i})^2)} + \ln(\sigma_j^2 + (\Delta V_{obs,i})^2) \right], \qquad (7)$$

where $V_{mod,i,j}$ is again given by equation (3) with $q_{kin,j} = q_{phot} = 0.87$. Symbols PA_i, $V_{obs,i}$ and $\Delta V_{obs,i}$ are the PA, recession velocity and uncertainty on the recession velocity for the i^{th} GC, respectively. We assume that the kinematic axial ratio of the GC system is equal to the photometric axial ratio of the galaxy light because the GC kinematic data do not constrain the kinematic axis (i.e. $q_{kin,j}$) ratio well.

Uncertainties on the fits to the GC kinematics are obtained using a bootstrapping method similar to that used by Côté et al. (2001). Basically, we obtain 1000 'mock' GC kinematic samples of 109 GCs (our actual sample size) by sampling with replacement from our measured distribution and fit each mock sample. The quoted uncertainties are the 68 per cent confidence interval inferred from the mock fits.

We also notice that this method tends to enhance the estimated rotation value when the PA varies as a free parameter. We used Monte Carlo methods to quantify this bias. We find that V_{rot} estimated using the above method on a sample of the same bin size and known slow rotation ($V_{rot} < 10$ km s^{-1}) can be enhanced by as much as 20 km s^{-1} when PA_{kin} is allowed to vary freely. This bias sharply reduces to $\lesssim$5 km s^{-1} for known input $V_{rot} > 50$ km s^{-1}. For this reason, fixing PA_{kin} to a reasonable value is recommended whenever possible to avoid this bias, especially when the output V_{rot} is low.

Table 4. List of spectroscopically identified contaminants and non-GC fillers. Columns 1 and 2 give the position in right ascension and declination (J2000), respectively. Columns 3, 4 and 5 are the Subaru/Suprime-Cam photometry. Measured recession velocities, when available, can be found in column 6. Column 7 lists the type of contaminant. The full table is available online – see Supporting Information.

α (hh:mm:ss) (1)	δ (hh:mm:ss) (2)	g_0 (mag) (3)	r_0 (mag) (4)	i_0 (mag) (5)	V_{obs} (km s^{-1} (6)	Type (7)
12:31:22.33	25:49:24.25	23.987 ± 0.029	23.312 ± 0.020	22.727 ± 0.020	–	galaxy
12:31:25.91	25:42:55.93	23.960 ± 0.023	23.512 ± 0.022	22.828 ± 0.020	–	galaxy
12:31:09.93	25:52:22.29	23.570 ± 0.021	22.813 ± 0.017	22.507 ± 0.018	–	galaxy
12:31:09.95	25:51:11.12	24.591 ± 0.027	24.331 ± 0.035	23.990 ± 0.031	–	galaxy
12:31:31.08	25:40:47.79	23.337 ± 0.020	22.927 ± 0.017	22.710 ± 0.019	–	galaxy
12:31:26.10	25:40:45.25	23.602 ± 0.021	23.360 ± 0.018	22.694 ± 0.018	–	galaxy
...	...	...	...	...	...	...

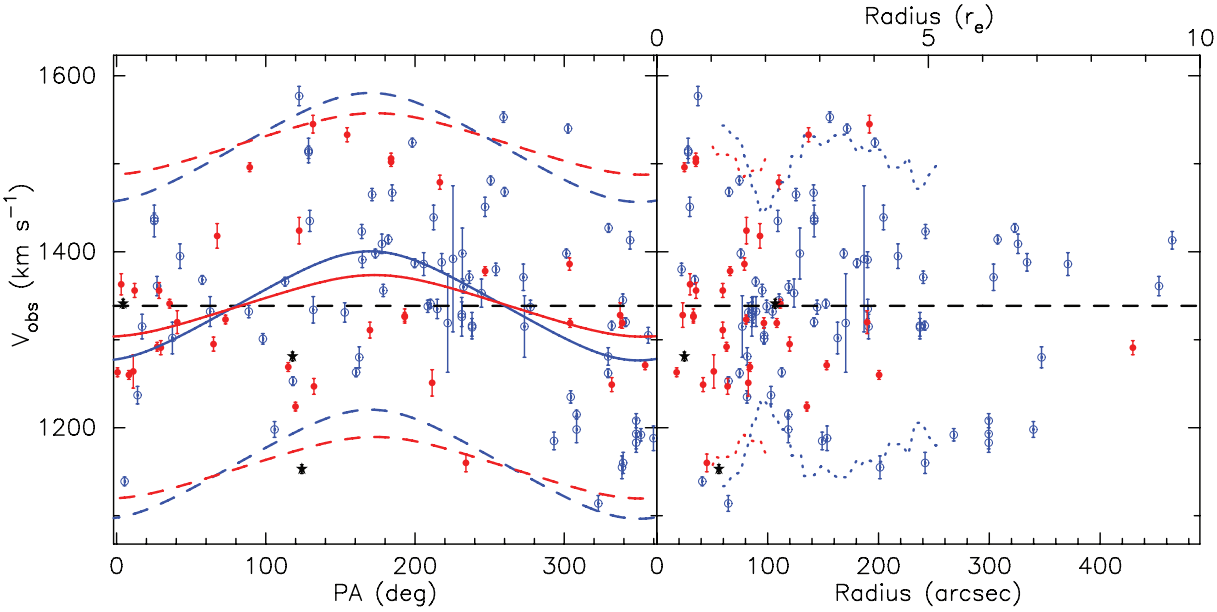

Figure 12. The GC velocity distribution of the blue (hollow blue symbols), red (filled red symbols) GCs and UCDs (star symbols) recession velocities as a function of PA (left panel) and galactocentric radius (right panel). Solid and dashed blue/red lines show the kinematic fit results and $\pm 2\sigma$, respectively, for the blue/red GC subpopulation. Blue/red dotted lines show $2\times$ the velocity dispersion (corrected for rotation) intervals for the blue/red GC subpopulation. Black dashed line represents NGC 4494's systemic velocity. The photometric PA is $PA_{kin} = 173°$. This figure is available in colour in the online version.

We find that the kinematic PA for the blue GCs (170^{+16}_{-14} deg) is consistent with the photometric PA in the inner parts of the galaxy measured by N09 (i.e. $PA_{phot} \sim 178°$, see Fig. 6). As will be discussed in great detail below, the red GCs show lower rotation, making the determination of the kinematic PA highly uncertain and artificially enhancing V_{rot}. Therefore, we fix the PA to the photometric PA (i.e. $PA_{kin,\,j} = PA_{phot}$) for both subpopulations in order to better constrain the other parameters. The resulting fits for our fiducial colour split are shown in Fig. 12 for the whole sample and rolling fits as a function of radius can be found in Fig. 6 for both GC subpopulations. We exclude GC88 from the radial rolling fits as its position at $>8r_e$ skews the measured rolling radius significantly. This does not change the amplitude of the fitted parameters significantly. We find significant major-axis rotation at all radii for the metal-poor GCs only with $41 \lesssim V_{rot} \lesssim 95$km s^{-1} (see Fig. 6). The metal-rich subpopulation may not show significant rotation as V_{rot} is consistent with 0 km s^{-1} at most radii. To test the effect of our colour split assumption, we perform rolling fits as a function of $(g - i)_0$ colour with moving bins of size 25, which we show in Fig. 13. These demonstrate that intermediate colour GCs [i.e. $0.90 < (g - i)_0 < 0.98$], in particular, do not show significant rotation and that this results in a higher uncertainty on the kinematic PA. This peculiarity is yet another hint of a possible third intermediate colour GC subpopulation around NGC 4494. On the other hand, the reddest GCs [$(g - i)_0 > 0.98$] tentatively show some rotation. In every case we find that the velocity dispersion (σ) of all subpopulations is consistent with each other (see Fig. 6).

3.2.4 *GC metallicities*

We are able to measure spectroscopic metallicities for 54 individual GCs and the three UCDs around NGC 4494 using the CaT and the method described in F10. Briefly, we fit the GC spectra using the pPXF routine described in Cappellari & Emsellem (2004) to obtain a template of our GC spectra. We use the set of templates described in Section 3.2.3 (example fits are shown in Fig. 2). Next, the fitted spectra are continuum normalized using the IRAF routine CONTINUUM with a spline3 function of the order of ∼4 and a stricter lower sigma clipping to avoid spectral features being fitted. The CaT index defined in F10 (CaT_{F10}, see Table 5) is measured on the template-fitted and continuum-normalized spectra. We emphasize that this

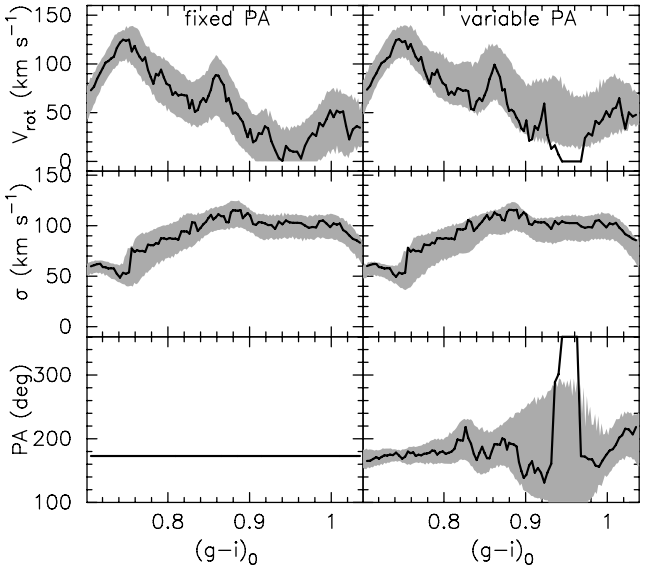

Figure 13. Rolling colour fits to the GC kinematics. Two cases are presented: $PA_{kin} = PA_{phot}$ (left panels) and variable PA_{kin} (right panels). Shaded areas represent 68 per cent confidence intervals.

Table 5. CaT index definition for galaxy stellar light spectra (CaT_{F09}) and GC spectra (CaT_{F10}).

Passband	CaT_{F10} (Å)	CaT_{F09} (Å)
Ca1	8490.0–8506.0	8483.0–8513.0
Ca2	8532.0–8552.0	8527.0–8557.0
Ca3	8653.0–8671.0	8647.0–8677.0
		8474.0–8483.0
		8514.0–8526.0
Shared continuum		8563.0–8577.0
		8619.0–8642.0
		8680.0–8705.0

CaT_{F10} is different from CaT_{F09} used above for galaxy spectra, which has broader passbands to accommodate the broadening of the CaT features due to large velocity dispersion in galaxies. The CaT_{F10} indices are transformed into metallicity using the following equation:

$$[Fe/H] = -3.641 + 0.438 \times CaT_{F10} \quad (8)$$

based on the empirical conversion of Armandroff & Zinn (1988) derived from the integrated light spectra of Galactic GCs. For more information on this technique, see F10.

Fig. 14 shows our measured CaT_{F10} index as a function of $(g - i)_0$ colour. We keep multiple CaT_{F10} measurements of individual objects as separate data points. Predictions from the V03 and Bruzual & Charlot (2003) SSP models are overlaid for comparison.

There are several immediately striking features in Fig. 14. First of all, the correlation between the CaT_{F10} and colour is obvious and consistent with linear, albeit with large observational scatter. There is one outlier, namely the faint ($i_0 = 21.8$) red GC, GC102. There is nothing obviously wrong with the photometry or spectrum (fitted or raw) of GC102, so we cannot explain the position of this (low signal-to-noise ratio) outlier in Fig. 14.

The bulk of the GC data lie above the Bruzual & Charlot (2003) SSP models and close to those of V03 (for bluer colours). The apparently linear relationship found in NGC 4494 data up to the reddest colours is in contrast to the findings of F10 for the giant elliptical galaxy NGC 1407, where the generally redder data follow the 13 Gyr V03 model track more closely at all colours. Many blue/red GCs in NGC 1407 have higher/lower measured CaT_{F10} indices than the NGC 4494 GCs. We discuss this discrepancy and its implications for using the CaT as a metallicity indicator for extragalactic GCs in Appendix B.

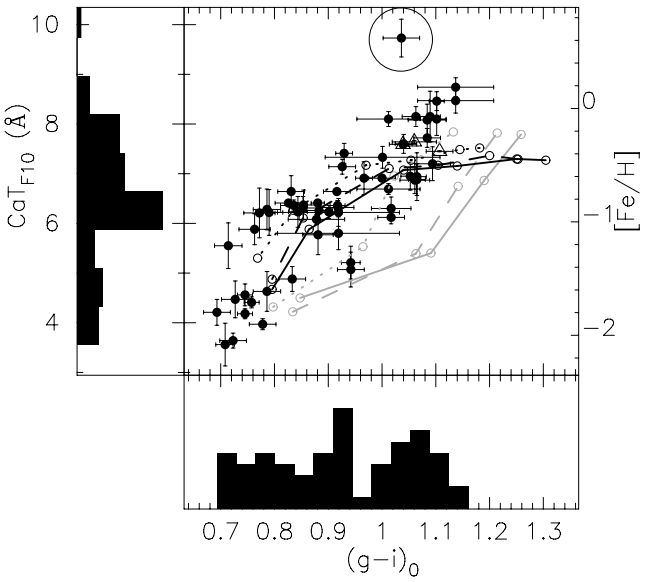

Figure 14. CaT_{F10} and inferred metallicity (right *y*-axis) as a function of colour for GCs (filled circles) and UCDs (hollow triangles) around NGC 4494. All repeat CaT_{F10} measurements of individual objects are shown. Histograms for each axis are also shown. One outlier (highlighted with a large hollow circle) is discussed in the text. Predictions from the SSP models of V03 (black) and Bruzual & Charlot (2003, grey) are shown for 5 (dotted line), 9 (dashed line) and 13 (solid line) Gyr.

Finally, there appears to be a concentration of GCs with $CaT_{F10} \sim 6.5$ Å (or $[Fe/H] \sim -0.9$). While our sample of spectroscopic GC metallicities is rather small for inferring the global properties of the distribution of GC metallicities in NGC 4494, it appears to be single peaked despite exhibiting clear $(g - i)_0$ colour bimodality (KMM yields a p-value of 0.002 for the confirmed GC sample). We note, however, that KMM is less reliable for small samples (see Ashman et al. 1994). Nevertheless, it is puzzling that the peak in the CaT distribution corresponds to the trough of the colour distribution (see Fig. 14). This result is reminiscent of that obtained for NGC 1407 (F10) and Caldwell et al. (2011), where the clear colour bimodality also translated into a skewed single-peaked spectroscopic metallicity distribution.

3.2.5 Three UCDs around NGC 4494

As briefly mentioned in Section 3.2.1, we report the discovery of three spectroscopically confirmed UCDs (Drinkwater et al. 2000) associated with NGC 4494. We adopt a magnitude definition for UCDs of $M_i < -10.9$, roughly equivalent to that adopted by Evstigneeva et al. (2008) in the *V* band. The three UCDs have absolute *i*-band magnitudes of −11.88, −11.92 and −11.71 mag, well within the range for UCD luminosities. Most UCDs have typically been found in dense cluster environments although, for example, one UCD has been confirmed around the Sombrero galaxy (Spitler et al. 2006; Hau et al. 2009), a spiral galaxy in a low-density environment. Another relevant example is that of NGC 5128, also

an $L*$ ETG, wherein several possible UCDs may have been found (Taylor et al. 2010).

There is ongoing discussion in the literature about the origin and definition of UCDs. Popular formation scenarios propose that UCDs are either (1) the bright end of the compact star cluster (i.e. GC) luminosity function (e.g. Mieske, Hilker & Infante 2004), or (2) the slightly more extended remnants of tidally stripped dwarf galaxies (Bekki et al. 2003). Of course, both scenarios may occur (see Da Rocha et al. 2011; Norris & Kannappan 2011). We thus examine the properties of the UCDs around NGC 4494 in order to determine their most likely origin.

UCD1 and UCD2 are within the *HST* imaging. We measure their sizes using ISHAPE (Larsen 1999) and obtain 1.7 ± 0.4 and 2.3 ± 0.6 pc for UCD1 and UCD2, respectively. We are unable to obtain a size estimate for UCD3 as it is unresolved on the Subaru image. Therefore, at least two of the three UCDs around NGC 4494 are compact, as predicted by the star cluster origin scenario. All three UCDs have high CaT-inferred metallicities ($-0.3 \gtrsim$ [Fe/H] $\gtrsim -0.4$) as is also the case for some other UCDs (e.g. Evstigneeva et al. 2007). UCD1 is detected with *Chandra* in the X-ray (Humphrey & Buote 2008, object ID NGC_4494_CXOU_12:3125.5+254619) with $L_{\rm X} = (2.1 \pm 1.1) \times 10^{38}$ erg s^{-1}. This X-ray luminosity is consistent with the presence of low-mass X-ray binary stars in UCD1.

Following Da Rocha et al. (2011), we compute the number of expected GCs brighter than $i_0 = 19.3$ (i.e. the magnitude of our faintest UCD candidate) around NGC 4494 assuming that UCDs around NGC 4494 are simply the bright end of its GC system. We use the total number of GCs and the GC luminosity function (Kundu & Whitmore 2001) to estimate that 2 ± 2 UCDs are consistent with being the bright extension of the GC system. Thus, under these assumptions, our three confirmed UCDs brighter than $i_0 = 19.3$ around NGC 4494 are consistent with representing the bright end of the GC luminosity function. We conclude that there is no need to invoke another formation channel such as tidal stripping of dwarf galaxies (e.g. Norris & Kannappan 2010; Da Rocha et al. 2011) for the UCDs around NGC 4494.

4 DISCUSSION

In this section, we compare the observed properties of NGC 4494 with the predictions from theoretical models in order to get an understanding of its formation.

4.1 Inferences from the stellar light

In Section 3.1.2 we report a 'flattening' of the stellar kinematics of NGC 4494 with radius such that the kinematics become more discy at large radii. In other words, at large radii only the stars close to the semimajor axis show rotation such that the kinematic axial ratio $q_{\rm kin}$ is low. This is supported by the observed anti-correlation between h_3 and $(V_{\rm obs} - V_{\rm sys})/\sigma$, which indicates the presence of a disc-like structure. However, it contrasts with the stellar surface brightness of the galaxy, which has a very constant and relatively round profile at all radii. This kinematic flattening at large radii may be related to the transition suggested by Hoffman et al. (2010) between 1 and 3 $r_{\rm e}$, where the kinematic signature of the progenitors' disc stars survived. However, it is a puzzle as to how such a 'kinematic' disc at large radii could be invisible in the imaging data. Indeed, the axial ratio of kinematic sub-structures are usually found to agree with that of the stellar distribution (e.g. Krajnović et al. 2008).

The stellar populations do not show any hint of a flattened distribution either. Denicoló et al. (2005) reported a central age of 6.7 Gyr with a central metallicity of [Fe/H] $\approx +0.03$ dex for NGC 4494 and F09 find no evidence for radial metallicity variations with metallicities roughly constant around [Fe/H] $\gtrsim -0.5$ dex between $\sim$0.2 and $1.4 r_{\rm e}$. In this work, we find no azimuthal variations in the measured CaT index values (see Fig. 8) or colour. The CaT gradient suggests that the luminosity-weighted metallicity of the NGC 4494 stars is higher than ~ -0.5 dex from $0.2 r_{\rm e}$ all the way out to at least $\sim 1.6\ r_{\rm e}$ and/or that the metallicity gradient is undetectably shallow for the CaT method. The colour gradient in the same radial range suggests a moderate metallicity gradient of $\sim -0.17 \pm 0.02$ dex per dex.

Recently, the SAURON team reported the results of their 2D stellar population analysis on 48 ETGs (Kuntschner et al. 2010). They find that flattened structures in the images of fast-rotators (Emsellem et al. 2007; Krajnović et al. 2008) with discy kinematics have distinct stellar populations, while galaxies classified as slow-rotators, and sometimes *harbouring inner kinematically decoupled cores*, show no clearly distinct stellar population variation. NGC 4494 does not appear to fit either of those categories. At small radii $\sim 0.1 r_{\rm e}$, the kinematically decoupled core suggests it is a slow-rotator. At all other radii, its increasingly flattened kinematics suggest it is a fast-rotator, but as stated above we find no evidence for a flattening of the stellar distribution or of distinct stellar populations from either the $\rm CaT_{F09}$ or the modelling of the surface brightness profile and colours. In any case, transitions between slow- and fast-rotators at large radii may be common as P09 also report a transition from a fast to a slow-rotator beyond the SAURON field of view in NGC 821. Again, these may be the first observational evidence for the transitional kinematics expected to occur between 1 and $3 r_{\rm e}$ in major merger remnants (Hoffman et al. 2010).

In Fig. 15, we plot a standard $\langle V_{\rm rot}/\sigma \rangle$ versus $\epsilon = 1 - q_{\rm phot}$ diagnostic diagram (Cappellari et al. 2007). This plot can be used to diagnose both the intrinsic structure of the galaxy (in particular NGC 4494) and the nature of the merger. We have highlighted NGC 4494 on this diagram showing the ATLAS3D data (Emsellem et al. 2011). The green curve in Fig. 15 represents an oblate isotropic rotator seen edge-on, and the magenta curve shows what is typical for an edge-on fast-rotator after modelling the dynamics of the SAURON sample as inferred by Cappellari et al. (2007). Because galaxies are generally observed *below* the green curve, this suggests that they are *not* isotropic. These results allow us to derive a best-guess solution for the inclination of any fast-rotator (including NGC 4494) by assuming that its internal anisotropy follows the mean trend of the other galaxies. We can also thereby estimate the ellipticity and $\langle V_{\rm rot}/\sigma \rangle$ values that would be obtained if the galaxy was viewed *edge-on*.

The black curve shows the track of possible edge-on values for NGC 4494 for a series of different inclinations, where we note that the dependence of the dispersion on inclination enters through the assumed anisotropy. The intersection of the black curve with the magenta curve then represents the self-consistent solution for NGC 4494 under the SAURON-based anisotropy assumption. From this we conclude that NGC 4494 is *most likely* (but not definitively) a flattened galaxy ($q_{\rm phot} \sim 0.6$) seen at an inclination of $\sim 45^\circ$. It may even be an S0 rather than a bona fide elliptical. The uncertainties here are driven not by the measured parameters (which are determined very precisely) but by the intrinsic scatter in the anisotropy–ellipticity relation. To estimate this, we use the spread of observed galaxies to the right of the magenta curve in Fig. 15. This suggests an intrinsic ellipticity uncertainty of $\sim \pm 0.2$, and an inclination between 39° and 90°. Similarly, using 2D dynamical modelling of NGC 4494, Rodionov & Athanassoula (2011) found

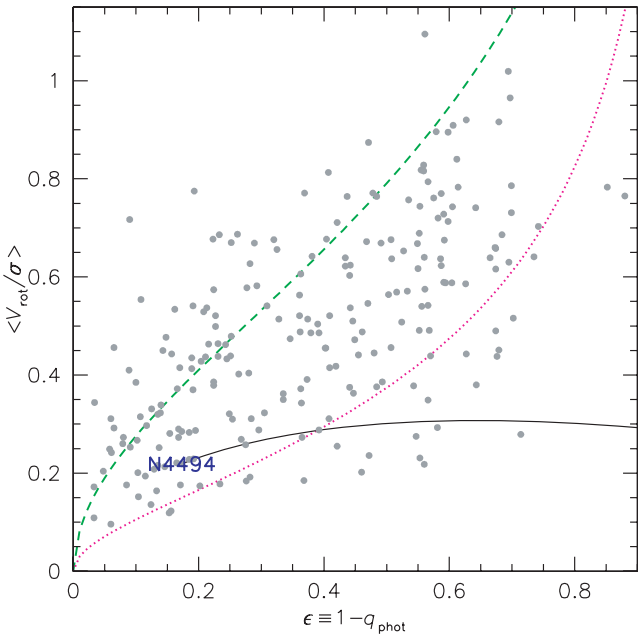

Figure 15. Azimuthally averaged rotation $\langle V_{\rm rot}/\sigma \rangle$ versus ellipticity ($\epsilon = 1 - q_{\rm phot}$) diagnostic diagram, after Cappellari et al. (2007). Data points represent the central regions of nearby ETGs classified as 'fast-rotators' from the SAURON and ATLAS3D surveys. The green dashed curve shows a theoretical prediction for edge-on oblate isotropic rotators, and the magenta dotted curve shows the inferred edge-on average relation for nearby fast-rotators. The observed position of NGC 4494 in the diagram is labelled, with a solid black curve showing the path of possible intrinsic values for a sequence of different assumed inclination angles. This figure is available in colour in the online version.

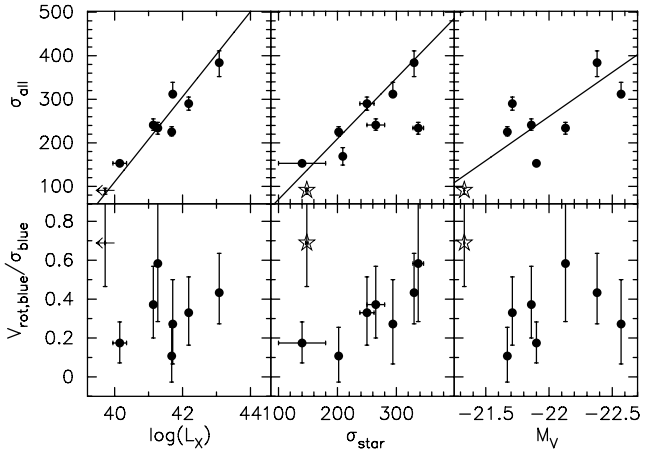

Figure 16. Comparison of salient GC kinematic properties with host galaxy global parameters: X-ray luminosity [$\log(L_{\rm X})$], stellar velocity dispersion ($\sigma_{\rm star}$) and absolute V-band magnitude (M_V). Symbols on the y-axis and GC kinematics are from Table 6. We include literature GC kinematic studies (filled circles) and NGC 4494 data (hollow stars and upper limit symbols). Solid lines are bisector fits to correlated parameters from Lee et al. (2010, fig. 12). Datum for NGC 4494 disagrees with the $V_{\rm rot,blue}/\sigma_{\rm blue}$ versus $\sigma_{\rm star}$ trend observed in other large elliptical galaxies (middle lower panel).

that a $\sim$45° inclination may be preferred. If this interpretation is correct, then to recover edge-on $V_{\rm rot}$ estimates, all of our velocity estimates should be increased by $\sim$40 per cent.

4.2 Inferences from the GC system

We find that the GC colour subpopulations are reasonably well defined in NGC 4494 and choose a nominal colour cut at $(g - i)_0 = 0.99$ to delineate metal-poor from metal-rich GCs. The 54 spectroscopically measured GC metallicities vary between $-2.0\,{\rm dex} \lesssim {\rm [Fe/H]} \lesssim 0.0\,{\rm dex}$ and their distribution appears single-peaked around $[{\rm Fe/H}]_{\rm mean} \sim -1.0$ dex despite their clear bimodal colour distribution. A similar behaviour was found for GCs around NGC 1407 (F10) and M31 (Caldwell et al. 2011). These may have some interesting implications for the ubiquity of the GC metallicity bimodality as inferred from GC colour distributions (also see Yoon, Yi & Lee 2006; Peng et al. 2006; Blakeslee, Cantiello & Peng 2010).

It has been suggested (and shown) that the distribution of red GCs usually follows that of the galaxy stars, while blue GCs follow the X-ray halo profile of their host galaxy (e.g. Minniti 1996; Forbes et al. 2004; Boley et al. 2009). This suggestion is based on both model predictions and the similarities of the respective spatial distribution and abundances. Surprisingly, we find that the surface brightness profile of the stars does not compare well with the spatial distribution of the red (or the blue) GCs in NGC 4494 (see Fig. 11). Indeed, the Sersíc index of the stars is inconsistent with that of both GC subpopulations, and this difference is even more pronounced for the red GCs. A similar conclusion is reached from comparing the kinematics of the stars, which agrees better with the blue GC kinematics than with that of the red GCs at the same radius (see Fig. 6). On the other hand, the colour of the galaxy stars is consistent with that of the red GCs (see Fig. 8). Therefore, the association of the red GCs with the galaxy stars is less clear in NGC 4494 than previously observed in other galaxies.

In Section 3.2.3, we measure the rotational velocity and velocity dispersion of the blue and red GCs. In order to put our results into a broader context, Fig. 16 reproduces parts of fig. 12 from Lee et al. (2010) using the updated kinematic data presented in Table 6 and compares GC kinematics with the global properties of the host galaxies for large ETGs. One caveat of the following comparison has to do with the heterogeneity of the methods used in the various dynamical studies represented in Fig. 16. Moreover, NGC 4494 is the only fast-rotator with large GC kinematic sample. Thus, its GC kinematics may be intrinsically different. Nevertheless, we find that NGC 4494 compares well with other large ETGs. We confirm that it agrees with the trends found between the velocity dispersion of the whole GC system and X-ray, central galactic velocity dispersion and B-band absolute magnitude as reported in Lee et al. (2010). However, the kinematics of the blue GCs of NGC 4494 appear to deviate from that of other large elliptical galaxies in the $V_{\rm rot,blue}/\sigma_{\rm blue}$ versus $\sigma_{\rm star}$ space, emphasising the large rotation of the blue GCs. Perhaps surprisingly given the arguably 'unusually low' X-ray luminosity of NGC 4494, the GC kinematics agree well with the expected trend with galaxy X-ray luminosity (e.g. Romanowsky et al. 2003; O'Sullivan & Ponman 2004). This also suggests that the processes involved in the formation of NGC 4494 that led to its peculiar X-ray luminosity and kinematics have preserved the majority of the correlations between its global properties and its GC kinematics as with other large ETGs.

Assuming that NGC 4494 has indeed undergone a recent interaction as inferred by O'Sullivan & Ponman (2004) from its X-ray luminosity, then we may reasonably conclude that the bulk of its GC system formed before that interaction and is thus a conglomerate of the progenitors' GC systems. Therefore, the current GC kinematics may hold clues to the understanding of the kinematics of the progenitor galaxies involved in the latest merger event. In this spirit, we use numerical simulations of disc–disc major mergers in

Table 6. Compilation of salient GC kinematic properties in the literature for selected large ETGs (column 1). Rotation amplitudes for all, blue and red GCs are given in columns 2, 5 and 8, respectively. The PA of the rotation for all, blue and red GCs is given in columns 3, 6 and 9, respectively. Photometric PAs for each galaxy can be found in Table 1. The velocity dispersion for all, blue and red GCs is shown in columns 4, 7 and 10, respectively. The number of GCs in the kinematic sample for each study is shown in column 11. References in column 12 correspond to Côté et al. (2003, C03), Hwang et al. (2008, H08), Côté et al. (2001, C01), Schuberth et al. (2010, S10), Romanowsky et al. (2009, R09), Bergond et al. (2006, B06), Lee et al. (2010, L10) and Woodley et al. (2010a, W10a).

Galaxy	$V_{\rm rot,all}$ (km s^{-1})	$PA_{\rm kin,all}$ (○)	$\sigma_{\rm all}$ (km s^{-1})	$V_{\rm rot,blue}$ (km s^{-1})	$PA_{\rm kin,blue}$ (○)	$\sigma_{\rm blue}$ (km s^{-1})	$V_{\rm rot,red}$ (km s^{-1})	$PA_{\rm kin,red}$ (○)	$\sigma_{\rm red}$ (km s^{-1})	$N_{\rm GC}$	Reference
(1)	(2)	(3)	(4)	(5)	(6)	(7)	(8)	(9)	(10)	(11)	(12)
M49	53^{+52}_{-25}	105^{+45}_{-45}	312^{+27}_{-8}	93^{+69}_{-37}	100^{+37}_{-40}	342^{+33}_{-18}	12^{+76}_{-74}	195^{+56}_{-58}	265^{+34}_{-13}	263	C03
M60	141^{+50}_{-38}	225^{+12}_{-14}	234^{+13}_{-14}	130^{+62}_{-51}	218^{+16}_{-23}	223^{+13}_{-16}	171^{+58}_{-46}	237^{+18}_{-19}	258^{+21}_{-31}	121	H08
M87	169^{+42}_{-97}	66 ± 35	384^{+27}_{-32}	172^{+51}_{-108}	59 ± 52	397^{+37}_{-46}	160^{+120}_{-99}	76 ± 45	364^{+49}_{-52}	278	C01
NGC 1399	–	–	–	110 ± 53	130 ± 24	333 ± 16	61 ± 35	154 ± 33	239 ± 11	∼670	S10
NGC 1407	86^{+32}_{-39}	46^{+22}_{-21}	241^{+14}_{-12}	87^{+37}_{-57}	91^{+36}_{-32}	234^{+21}_{-16}	104^{+43}_{-53}	29^{+23}_{-28}	247^{+27}_{-17}	156	R09
NGC 3379	<100	–	169 ± 20	–	–	–	–	–	–	30	B06
NGC 4494	56^{+22}_{-5}	147^{+12}_{-18}	91^{+5}_{-9}	62^{+16}_{-11}	170^{+16}_{-14}	90^{+6}_{-9}	35^{+21}_{-20}	(173)[a]	92^{+8}_{-21}	109	this work
NGC 4636	37^{+32}_{-30}	174^{+73}_{-48}	225^{+12}_{-9}	27^{+34}_{-24}	0^{+146}_{-144}	251^{+18}_{-12}	68^{+48}_{-35}	178^{+53}_{-34}	203^{+12}_{-13}	238	L10
NGC 5128	33 ± 10	185 ± 15	–	26 ± 15	177 ± 28	149 ± 4	43 ± 15	196 ± 17	156 ± 4	564	W10a

[a]We fix $\rm PA_{kin} = PA_{phot} = 173^{\circ}$ to get a better handle on the red GC kinematics since the rotation is low (see text).

order to see what can be learned about the progenitors from the GC kinematics. Details of the simulations and results are presented in Appendix C. By studying numerous simulations of mergers with a variety of initial conditions, we find that the model that best reproduces the observed kinematics of the blue and red GCs (ignoring the intermediate colour GCs that show little rotation) involves a major disc–disc merger with a large amount of orbital angular momentum and a retrograde–retrograde orbital configuration. Models with other orbital configurations do not yield GC kinematics that are consistent with what is observed for NGC 4494. This is a suggestion that NGC 4494 may be a major merger remnant.

5 SUMMARY AND CONCLUSIONS

NGC 4494 has often been dubbed an 'ordinary elliptical' galaxy, making it an ideal target for understanding the formation and evolution of a typical galaxy. In this work, we combine imaging and spectroscopy of stellar light and GCs in NGC 4494. From the imaging we obtain the stellar surface brightness profiles and GC density profiles. We find that the colour distribution of the GC system around NGC 4494 is statistically better fitted by two Gaussians than a single one suggesting metallicity bimodality. The spectroscopy yields spatially resolved kinematics and abundances of the stellar component and GCs. A total of 109 individual GCs and three UCD/DGTOs are confirmed spectroscopically. The properties of the UCDs are consistent with them being bright GCs. Metallicities are measured for 54 GCs and the three UCDs using the CaT absorption lines. The CaT-inferred metallicity distribution for the GC system is single-peaked, in contrast to that inferred from the colours, which is clearly bimodal. Measurements for both the stellar light and GC spectroscopy can be found in Appendix A. We find that while the intermediate colour (green) GCs do not rotate, the blue (and possibly reddest) GCs do rotate (Fig. 13) as do the galaxy stars (Fig. 6). The velocity dispersion of all GC subpopulations and the galaxy stars are consistent.

A comparison of the GC system's kinematics and the global properties of NGC 4494 with those of other large ETGs suggests that NGC 4494 is indeed typical with the exception of the unusually high blue GC rotation. We find suggestive evidence in the distinct kinematics for a possible third intermediate colour (green) GC subpopulation. We infer that most of the observational evidence suggests that NGC 4494 is consistent with formation via a recent *gas-rich* major merger, but other formation scenarios cannot be ruled out. Some remaining open issues are as follows.

(i) The relatively old (6.7 Gyr) measured central age suggests that little dissipation and recent central star formation have occurred (i.e. possibly a dry merger). However, its cuspy surface brightness profile and the presence of a kinematically decoupled core suggest a high gas fraction of $\gtrsim$15 per cent (Hopkins et al. 2009; Hoffman et al. 2010). This is also supported by the presence of an inner dust ring (Xu, Narayanan & Walker 2010). Therefore, the evidence is not conclusive as to the amount of gas dissipation involved in the formation of NGC 4494. The possibly 'unusually' low X-ray luminosity suggests that the mechanism involved in depleting the gas must have allowed enough dissipation to form a kinematically decoupled core without significant recent central star formation.

(ii) The inner kinematic profile of NGC 4494 follows the light profile well up to $\sim 1.8 r_{\rm e}$, beyond that the kinematics become increasingly flattened with radius (i.e. the axial ratio $q_{\rm kin}$ is low). We find no evidence of a flattened component in the stellar distribution from our imaging. It is, however, not surprising to find transitions in the kinematics of merger remnants at 1–3$r_{\rm e}$ as they are predicted in the models of Hoffman et al. (2010). We suggest that NGC 4494 may be a flattened galaxy ($q_{\rm phot} = 0.6 \pm 0.2$), possibly even an S0, seen at an inclination of 45^{+45}_{-6} deg based on its position in the classic $\langle V_{\rm rot}/\sigma \rangle$ versus $\epsilon = 1 - q_{\rm phot}$ diagram (Fig 15). This may explain its high flattened rotation with round photometric isophotes.

Off-axis deep optical spectroscopy out to large galactocentric radii would be a good way to independently test the flattened kinematics. It would also allow for a stellar population analysis (i.e. ages, metallicities and α-element abundances) using the standard and well-tested Lick system (e.g. Proctor & Sansom 2002). The added knowledge of spatially resolved stellar ages and α-element abundances may highlight distinct stellar populations as observed by SAURON (Kuntschner et al. 2010) that were not seen from our near-infrared spectra.

This work shows that such complete studies of individual galaxies incorporating as many lines of evidence as available can help

disentangle the processes involved in the formation and evolution of selected galaxies. As such data sets become available, observational constraints based on statistical samples will help improve our understanding of the details of galaxy formation and evolution.

ACKNOWLEDGMENTS

We would like to thank the anonymous referee for his/her careful reading of our manuscript and helpful comments. Soeren Larsen is acknowledged for providing us with the *HST*/WFPC2 GC catalogue. We thank Michele Cappellari and Loren Hoffman for helpful discussions. CF thanks the Anglo-Australian Observatory for financial support in the form of a graduate top-up scholarship. DAF thanks the ARC for financial support. JPB and AJR acknowledge support from NSF grant AST-0808099 and AST-0909237. Based in part on data collected at Subaru Telescope and obtained from the SMOKA, which is operated by the Astronomy Data Center, National Astronomical Observatory of Japan. Part of the Subaru data analysed was obtained through a Gemini time exchange, program GN-2008A-C-12. The data presented herein were obtained at the W.M. Keck Observatory, which is operated as a scientific partnership among the California Institute of Technology, the University of California and the National Aeronautics and Space Administration. The Observatory was made possible by the generous financial support of the W.M. Keck Foundation. The analysis pipeline used to reduce the DEIMOS data was developed at UC Berkeley with support from NSF grant AST-0071048. We acknowledge the usage of the HyperLeda data base (http://leda.univ-lyon1.fr) and of NED, which is operated by the Jet Propulsion Laboratory, California Institute of Technology, under contract with the National Aeronautics and Space Administration. This publication makes use of data products from the Two Micron All Sky Survey, which is a joint project of the University of Massachusetts and the Infrared Processing and Analysis Center/California Institute of Technology, funded by the National Aeronautics and Space Administration and the National Science Foundation.

REFERENCES

Abazajian K. N. et al., 2009, ApJS, 182, 543
Armandroff T. E., Zinn R., 1988, AJ, 96, 92
Ashman K. M., Zepf S. E., 1992, ApJ, 384, 50
Ashman K. M., Bird C. M., Zepf S. E., 1994, AJ, 108, 2348
Bassino L. P., Richtler T., Dirsch B., 2006, MNRAS, 367, 156
Beasley M. A., Baugh C. M., Forbes D. A., Sharples R. M., Frenk C. S., 2002, MNRAS, 333, 383
Bekki K., 2010, MNRAS, 401, 2753
Bekki K., Shioya Y., 1999, ApJ, 513, 108
Bekki K., Forbes D. A., Beasley M. A., Couch W. J., 2002, MNRAS, 335, 1176
Bekki K., Couch W. J., Drinkwater M. J., Shioya Y., 2003, MNRAS, 344, 399
Bekki K., Beasley M. A., Brodie J. P., Forbes D. A., 2005, MNRAS, 363, 1211
Bell E. F., McIntosh D. H., Katz N., Weinberg M. D., 2003, ApJS, 149, 289
Bender R., Saglia R. P., Gerhard O. E., 1994, MNRAS, 269, 785
Bergond G., Zepf S. E., Romanowsky A. J., Sharples R. M., Rhode K. L., 2006, A&A, 448, 155
Bica E., Alloin D., 1987, A&A, 186, 49
Blakeslee J. P., Cantiello M., Peng E. W., 2010, ApJ, 710, 51
Boley A. C., Lake G., Read J., Teyssier R., 2009, ApJ, 706, L192
Brodie J. P., Strader J., 2006, ARA&A, 44, 193
Brodie J. P., Strader J., Denicoló G., Beasley M. A., Cenarro A. J., Larsen S. S., Kuntschner H., Forbes D. A., 2005, AJ, 129, 2643
Bruzual G., Charlot S., 2003, MNRAS, 344, 1000
Burkert A., Tremaine S., 2010, ApJ, 720, 516
Caldwell N., Schiavon R., Morrison H., Rose J. A., Harding P., 2011, AJ, 141, 61
Capaccioli M., Caon N., D'Onofrio M., 1992, MNRAS, 259, 323
Cappellari M., Emsellem E., 2004, PASP, 116, 138
Cappellari M. et al., 2007, MNRAS, 379, 418
Cenarro A. J., Beasley M. A., Strader J., Brodie J. P., Forbes D. A., 2007, AJ, 134, 391
Cenarro A. J., Cardiel N., Gorgas J., 2008, in Knapen J. H., Mahoney T. J., Vazdekis A., eds, ASP Conf. Ser. Vol. 390, Pathways Through an Eclectic Universe. The Calcium Triplet Gradient of M32. Astron. Soc. Pac., San Francisco, p. 292
Coccato L. et al., 2009, MNRAS, 394, 1249
Côté P. et al., 2001, ApJ, 559, 828
Côté P., McLaughlin D. E., Cohen J. G., Blakeslee J. P., 2003, ApJ, 591, 850
Da Rocha C., Mieske S., Georgiev I. Y., Hilker M., Ziegler B. L., Mendes de Oliveira C., 2011, A&A, 525, A86
de Vaucouleurs G., 1953, MNRAS, 113, 134
de Vaucouleurs G., de Vaucouleurs A., Corwin H. G., Jr, Buta R. J., Paturel G., Fouque P., 1991, Third Reference Catalogue of Bright Galaxies. Springer, New York
Denicoló G., Terlevich R., Terlevich E., Forbes D. A., Terlevich A., 2005, MNRAS, 358, 813
Di Matteo P., Pipino A., Lehnert M. D., Combes F., Semelin B., 2009, A&A, 499, 427
Diaz A. I., Terlevich E., Terlevich R., 1989, MNRAS, 239, 325
Dirsch B., Richtler T., Geisler D., Forte J. C., Bassino L. P., Gieren W. P., 2003, AJ, 125, 1908
Drinkwater M. J., Jones J. B., Gregg M. D., Phillipps S., 2000, Proc. Astron. Soc. Aust., 17, 227
Dufour R. J., Harvel C. A., Martins D. M., Schiffer F. H., III, Talent D. L., Wells D. C., van den Bergh S., Talbot R. J., Jr, 1979, AJ, 84, 284
Emsellem E. et al., 2004, MNRAS, 352, 721
Emsellem E. et al., 2007, MNRAS, 379, 401
Emsellem E. et al., 2011, MNRAS, 414, 888
Evstigneeva E. A., Gregg M. D., Drinkwater M. J., Hilker M., 2007, AJ, 133, 1722
Evstigneeva E. A. et al., 2008, AJ, 136, 461
Feigelson E. D., Babu G. J., 1992, ApJ, 397, 55
Forbes D. A., Franx M., Illingworth G. D., Carollo C. M., 1996, ApJ, 467, 126
Forbes D. A., Grillmair C. J., Williger G. M., Elson R. A. W., Brodie J. P., 1998, MNRAS, 293, 325
Forbes D. A. et al., 2004, MNRAS, 355, 608
Foster C., Proctor R. N., Forbes D. A., Spolaor M., Hopkins P. F., Brodie J. P., 2009, MNRAS, 400, 2135
Foster C., Forbes D. A., Proctor R. N., Strader J., Brodie J. P., Spitler L. R., 2010, AJ, 139, 1566 (F10)
Graham A. W., Driver S. P., 2005, Proc. Astron. Soc. Aust., 22, 118
Harris W. E., 2009, ApJ, 703, 939
Harris G. L. H., Harris W. E., 2011, MNRAS, 410, 2347
Harris W. E., van den Bergh S., 1981, AJ, 86, 1627
Hau G. K. T., Spitler L. R., Forbes D. A., Proctor R. N., Strader J., Mendel J. T., Brodie J. P., Harris W. E., 2009, MNRAS, 394, L97
Hoffman L., Cox T. J., Dutta S., Hernquist L., 2010, ApJ, 723, 818
Hopkins P. F., Cox T. J., Dutta S. N., Hernquist L., Kormendy J., Lauer T. R., 2009, ApJS, 181, 135
Hopkins P. F. et al., 2010, ApJ, 715, 202
Humphrey P. J., Buote D. A., 2008, ApJ, 689, 983
Hwang H. S. et al., 2008, ApJ, 674, 869
Jensen J. B., Tonry J. L., Barris B. J., Thompson R. I., Liu M. C., Rieke M. J., Ajhar E. A., Blakeslee J. P., 2003, ApJ, 583, 712
Jorgensen U. G., Carlsson M., Johnson H. R., 1992, A&A, 254, 258
Kissler-Patig M., Gebhardt K., 1998, AJ, 116, 2237
Kobayashi C., Arimoto N., 1999, ApJ, 527, 573
Koch A., Grebel E. K., Wyse R. F. G., Kleyna J. T., Wilkinson M. I., Harbeck D. R., Gilmore G. F., Evans N. W., 2006, AJ, 131, 895

Krajnović D., Cappellari M., de Zeeuw P. T., Copin Y., 2006, MNRAS, 366, 787
Krajnović D. et al., 2008, MNRAS, 390, 93
Krajnovic D. et al., 2011, MNRAS, in press (arXiv:1102.3801)
Kundu A., Whitmore B. C., 2001, AJ, 121, 2950
Kuntschner H. et al., 2010, MNRAS, 408, 97
Lackner C. N., Ostriker J. P., 2010, ApJ, 712, 88
Larsen S. S., 1999, A&AS, 139, 393
Larsen S. S., Brodie J. P., Huchra J. P., Forbes D. A., Grillmair C. J., 2001, AJ, 121, 2974
Lauer T. R. et al., 2005, AJ, 129, 2138
Lauer T. R. et al., 2007, ApJ, 664, 226
Lee M. G., Park H. S., Hwang H. S., Arimoto N., Tamura N., Onodera M., 2010, ApJ, 709, 1083
López-Sanjuan C., Balcells M., Pérez-González P. G., Barro G., García-Dabó C. E., Gallego J., Zamorano J., 2010, ApJ, 710, 1170
Mieske S., Hilker M., Infante L., 2004, A&A, 418, 445
Minniti D., 1996, ApJ, 459, 175
Miyazaki S. et al., 2002, PASJ, 54, 833
Muratov A. L., Gnedin O. Y., 2010, ApJ, 718, 1266
Napolitano N. R. et al., 2009, MNRAS, 393, 329 (N09)
Norris M. A., Kannappan S. J., 2010, preprint (arXiv:1009.2489)
Norris M. A., Kannappan S. J., 2011, MNRAS, 414, 739
Norris M. A. et al., 2008, MNRAS, 385, 40
O'Sullivan E., Ponman T. J., 2004, MNRAS, 349, 535
Ouchi M. et al., 2004, ApJ, 611, 660
Paturel G., Petit C., Prugniel P., Theureau G., Rousseau J., Brouty M., Dubois P., Cambrésy L., 2003, A&A, 412, 45
Peng E. W. et al., 2006, ApJ, 639, 95
Peng E. W. et al., 2008, ApJ, 681, 197
Peng E. W. et al., 2011, ApJ, 730, 23
Pipino A., D'Ercole A., Chiappini C., Matteucci F., 2010, MNRAS, 407, 1347
Proctor R. N., Sansom A. E., 2002, MNRAS, 333, 517
Proctor R. N., Forbes D. A., Brodie J. P., Strader J., 2008, MNRAS, 385, 1709
Proctor R. N., Forbes D. A., Romanowsky A. J., Brodie J. P., Strader J., Spolaor M., Mendel J. T., Spitler L., 2009, MNRAS, 398, 91 (P09)
Puzia T. H., Kissler-Patig M., Thomas D., Maraston C., Saglia R. P., Bender R., Goudfrooij P., Hempel M., 2005, A&A, 439, 997
Reda F. M., Proctor R. N., Forbes D. A., Hau G. K. T., Larsen S. S., 2007, MNRAS, 377, 1772
Rodionov S. A., Athanassoula E., 2011, MNRAS, 410, 111
Romanowsky A. J., Douglas N. G., Arnaboldi M., Kuijken K., Merrifield M. R., Napolitano N. R., Capaccioli M., Freeman K. C., 2003, Sci, 301, 1696
Romanowsky A. J., Strader J., Spitler L. R., Johnson R., Brodie J. P., Forbes D. A., Ponman T., 2009, AJ, 137, 4956
Sawilowsky S. S., 2007, Real Data Analysis. IAP Information Age Publishing, Charlotte, NC
Schlegel D. J., Finkbeiner D. P., Davis M., 1998, ApJ, 500, 525
Schuberth Y., Richtler T., Hilker M., Dirsch B., Bassino L. P., Romanowsky A. J., Infante L., 2010, A&A, 513, A52
Sérsic J. L., 1963, Boletin de la Asociacion Argentina de Astronomia La Plata Argentina, 6, 41
Sinnott B., Hou A., Anderson R., Harris W. E., Woodley K. A., 2010, AJ, 140, 2101
Skrutskie M. F. et al., 2006, AJ, 131, 1163
Snyder G. F., Hopkins P. F., Hernquist L., 2011, ApJ, 728, L24
Spitler L. R., Forbes D. A., 2009, MNRAS, 392, L1
Spitler L. R., Larsen S. S., Strader J., Brodie J. P., Forbes D. A., Beasley M. A., 2006, AJ, 132, 1593
Spitler L. R., Forbes D. A., Strader J., Brodie J. P., Gallagher J. S., 2008, MNRAS, 385, 361
Strader J., Brodie J. P., Cenarro A. J., Beasley M. A., Forbes D. A., 2005, AJ, 130, 1315
Taylor M. A., Puzia T. H., Harris G. L., Harris W. E., Kissler-Patig M., Hilker M., 2010, ApJ, 712, 1191
Tonry J. L., Dressler A., Blakeslee J. P., Ajhar E. A., Fletcher A. B., Luppino G. A., Metzger M. R., Moore C. B., 2001, ApJ, 546, 681
van den Bergh S., 1982, PASP, 94, 459
Vazdekis A., Cenarro A. J., Gorgas J., Cardiel N., Peletier R. F., 2003, MNRAS, 340, 1317 (V03)
West M. J., Côté P., Marzke R. O., Jordán A., 2004, Nat, 427, 31
White S. D. M., 1980, MNRAS, 191, 1p
Woodley K. A., Gómez M., Harris W. E., Geisler D., Harris G. L. H., 2010a, AJ, 139, 1871
Woodley K. A., Harris W. E., Puzia T. H., Gómez M., Harris G. L. H., Geisler D., 2010b, ApJ, 708, 1335
Worthey G., 1994, ApJS, 95, 107
Xu X., Narayanan D., Walker C., 2010, ApJ, 721, L112
Yagi M., Kashikawa N., Sekiguchi M., Doi M., Yasuda N., Shimasaku K., Okamura S., 2002, AJ, 123, 66
Yoon S., Yi S. K., Lee Y., 2006, Sci, 311, 1129
Zepf S. E., Ashman K. M., 1993, MNRAS, 264, 611

APPENDIX A: DATA TABLES

This section contains our measurements for the photometry, kinematics and stellar populations of stars and GCs in NGC 4494.

APPENDIX B: THE CAT AS A METALLICITY INDICATOR

In this section, we focus on the reliability of the CaT as a metallicity indicator for unresolved populations (i.e. GCs and galaxies). We use the data presented in this work to shed some light on two open issues.

First, the V03 SSP models predict that the CaT saturates at high metallicity (i.e. [Fe/H] $= -0.5$). This prediction is consistent with the distribution of the GC data for NGC 1407 in F10 but is less clear from Fig. 14 where the relationship between colour and CaT_{F10} appears linear at all probed metallicities. This is consistent with what has been observed in the Galactic GCs (Armandroff & Zinn 1988). On the other hand, in Fig. 8 the measured CaT_{F09} for galaxy spectra scatters about a constant value, which coincides with the saturation value predicted by the V03 models. This may be interpreted as proof of the saturation prediction. However, the galaxy colour gradient (see Fig. 4) is shallow at similar radii suggesting that the expected change in CaT_{F09} may be small. In other words, the absence of a CaT radial gradient in the galaxy found in this work and in F09 may not prove the V03 saturation prediction. The question remains open.

Second, F10 found that the brightest blue and red GCs in NGC 1407 have the same CaT index value despite their wide separation in colour. This casts serious doubt on the reliability of the CaT as a metallicity indicator. Moreover, several fitted GC spectra across the range of GC luminosities probed around NGC 1407 showed Paschen lines. We find no such Paschen lines in the GC spectra for NGC 4494, which cover a comparable range in absolute luminosities. The presence of Paschen features in the GCs around NGC 1407 cannot be confirmed directly on the raw spectra.

Several possible explanations for these behaviours are put forward in F10, including the presence of hot blue stars such as blue horizontal branch, blue straggler or young stars mainly in the blue GCs whose Paschen lines might be affecting the CaT features. Another possibility is that the CaT may saturate at lower metallicity (i.e. [Fe/H] ~ -0.8 dex) than predicted by V03 or perhaps colour does not trace metallicity linearly (e.g. Yoon et al. 2006; Peng et al. 2006; Blakeslee et al. 2010).

Based on the results for NGC 4494 shown in Fig. 14, there is no clear evidence that the CaT saturates earlier than predicted

Table A1. Individual values for NGC 4494 galaxy light. Columns 1 and 2 give the position of the individual slits in right ascension and declination (J2000), respectively. The observed velocity moments $V_{\rm obs}$, σ, h_3 and h_4 appear in columns 3, 4, 5 and 6. Measured values of the CaT index and [Fe/H] from the method of F09, when available, are shown in columns 7 and 8. We quote the maximum metallicity (i.e. [Fe/H] = +0.2) when the measured $\rm CaT_{F09}$ is higher than the metallicity range available in the V03 models. The errors on the quoted [Fe/H] values are based on the index errors only and do not include possible systematics due to the adopted calibration.

α (hh:mm:ss) (1)	δ (dd:mm:ss) (2)	$V_{\rm obs}$ (km s^{-1}) (3)	σ (km s^{-1}) (4)	h_3 (5)	h_4 (6)	$\rm CaT_{F09}$ (Å) (7)	[Fe/H] (dex) (8)
12:31:28.48	+25:44:22.64	1424.6 ± 32.8	193.5 ± 69.6	0.06 ± 0.04	0.02 ± 0.06	–	–
12:31:27.70	+25:45:00.50	1400.0 ± 13.3	131.2 ± 22.6	−0.01 ± 0.04	0.00 ± 0.05	––	–
12:31:29.85	+25:45:25.62	1351.1 ± 8.0	24.5 ± 12.9	−0.03 ± 0.04	−0.05 ± 0.09	–	–
12:31:28.52	+25:45:36.16	1350.6 ± 8.6	61.3 ± 18.6	0.01 ± 0.05	0.12 ± 0.08	–	–
12:31:35.35	+25:45:38.68	1295.1 ± 23.2	129.8 ± 23.9	−0.03 ± 0.03	−0.02 ± 0.04	–	–
12:31:32.23	+25:45:41.68	1366.3 ± 8.6	5.3 ± 10.5	0.00 ± 0.02	−0.01 ± 0.04	–	–
12:31:29.49	+25:45:59.14	1341.8 ± 9.6	90.3 ± 23.7	0.01 ± 0.03	0.05 ± 0.05	–	–
12:31:29.30	+25:46:16.30	1345.1 ± 6.8	63.1 ± 12.5	−0.02 ± 0.04	0.16 ± 0.20	–	–
12:31:30.76	+25:46:32.54	1326.6 ± 12.3	97.4 ± 13.2	−0.03 ± 0.04	0.00 ± 0.04	–	–
12:31:31.86	+25:46:44.74	1338.8 ± 11.3	53.7 ± 15.2	0.00 ± 0.03	−0.02 ± 0.02	–	–
12:31:33.12	+25:46:58.38	1397.9 ± 29.1	140.7 ± 46.1	0.06 ± 0.03	−0.03 ± 0.04	–	–
12:31:29.62	+25:47:01.63	1342.5 ± 11.9	115.7 ± 18.2	−0.08 ± 0.04	0.07 ± 0.05	–	–
12:31:29.23	+25:47:06.53	1319.5 ± 13.0	116.1 ± 18.3	0.01 ± 0.03	0.01 ± 0.03	–	–
12:31:27.03	+25:47:47.43	1305.1 ± 10.6	103.9 ± 13.2	0.02 ± 0.04	−0.02 ± 0.04	–	–
12:31:28.33	+25:48:33.16	1295.8 ± 13.3	37.4 ± 27.2	−0.01 ± 0.02	0.00 ± 0.02	–	–
12:31:26.95	+25:48:40.17	1228.3 ± 22.1	197.1 ± 19.4	−0.07 ± 0.03	0.01 ± 0.05	–	–
12:31:18.65	+25:44:25.92	1340.3 ± 18.0	53.0 ± 23.9	0.03 ± 0.02	−0.03 ± 0.02	–	–
12:31:26.03	+25:44:29.51	1393.7 ± 29.9	118.6 ± 49.5	−0.07 ± 0.06	0.00 ± 0.05	–	–
12:31:26.81	+25:44:44.90	1371.5 ± 28.1	98.7 ± 44.7	−0.04 ± 0.05	−0.01 ± 0.06	–	–
12:31:28.55	+25:44:57.96	1358.8 ± 19.3	112.5 ± 25.7	−0.05 ± 0.03	−0.01 ± 0.06	–	–
12:31:26.68	+25:45:02.68	1357.5 ± 19.0	94.4 ± 27.7	−0.07 ± 0.04	−0.03 ± 0.06	–	–
12:31:20.71	+25:45:07.73	1345.1 ± 14.0	94.0 ± 23.2	−0.03 ± 0.04	0.02 ± 0.05	–	–
12:31:26.78	+25:45:18.12	1373.2 ± 13.1	116.1 ± 20.1	−0.09 ± 0.04	0.03 ± 0.11	–	–
12:31:31.95	+25:45:28.89	1331.4 ± 14.0	92.3 ± 17.0	−0.02 ± 0.03	0.00 ± 0.03	–	–
12:31:31.42	+25:45:42.03	1340.8 ± 24.2	93.7 ± 27.9	−0.02 ± 0.02	0.00 ± 0.02	–	–
12:31:28.67	+25:45:50.66	1350.6 ± 10.3	105.1 ± 16.0	−0.08 ± 0.04	0.05 ± 0.12	–	–
12:31:29.11	+25:45:58.29	1332.5 ± 11.6	127.5 ± 16.0	−0.09 ± 0.04	−0.04 ± 0.07	–	–
12:31:23.50	+25:45:58.76	1400.4 ± 6.8	115.2 ± 10.5	−0.10 ± 0.03	0.07 ± 0.15	6.06 ± 0.40	−0.16 ± 1.48
12:31:27.86	+25:46:02.64	1344.1 ± 9.4	118.0 ± 12.6	−0.08 ± 0.04	−0.04 ± 0.11	6.94 ± 1.47	≥0.20
12:31:25.55	+25:46:13.94	1376.3 ± 6.3	137.7 ± 9.1	−0.07 ± 0.02	0.00 ± 0.09	6.19 ± 0.22	≥0.20
12:31:30.26	+25:46:18.45	1348.0 ± 11.5	73.3 ± 19.4	−0.02 ± 0.04	0.02 ± 0.05	–	–
12:31:25.51	+25:46:19.77	1360.0 ± 5.6	140.2 ± 8.5	−0.03 ± 0.01	−0.01 ± 0.04	6.28 ± 0.45	≥0.20
12:31:25.64	+25:46:30.60	1342.4 ± 5.6	141.2 ± 9.0	−0.04 ± 0.01	0.03 ± 0.07	6.35 ± 0.44	≥0.20
12:31:19.76	+25:46:37.36	1337.1 ± 12.6	134.1 ± 18.3	0.00 ± 0.04	0.07 ± 0.06	7.20 ± 1.35	≥0.20
12:31:25.94	+25:46:46.71	1316.3 ± 5.9	130.9 ± 9.0	−0.02 ± 0.02	−0.01 ± 0.02	6.49 ± 0.31	≥0.20
12:31:24.05	+25:46:48.18	1289.3 ± 5.3	144.1 ± 8.5	0.04 ± 0.01	−0.02 ± 0.05	6.25 ± 0.65	≥0.20
12:31:29.02	+25:46:50.84	1319.3 ± 10.1	115.4 ± 15.8	−0.02 ± 0.03	0.00 ± 0.05	8.14 ± 2.17	≥0.20
12:31:24.15	+25:47:00.18	1280.6 ± 5.5	129.0 ± 8.8	0.03 ± 0.02	0.02 ± 0.03	6.50 ± 0.20	≥0.20
12:31:19.67	+25:47:06.41	1326.2 ± 11.2	123.1 ± 12.2	−0.03 ± 0.04	−0.01 ± 0.05	8.69 ± 1.82	≥0.20
12:31:24.32	+25:47:10.83	1278.6 ± 6.1	120.9 ± 9.0	0.02 ± 0.03	0.01 ± 0.03	6.97 ± 0.45	≥0.20
12:31:19.46	+25:47:12.51	1309.2 ± 8.5	106.8 ± 13.0	−0.07 ± 0.04	0.03 ± 0.07	–	–
12:31:26.06	+25:47:23.55	1285.9 ± 10.1	124.3 ± 12.5	−0.08 ± 0.04	0.04 ± 0.07	7.83 ± 1.21	≥0.20
12:31:21.29	+25:47:32.93	1286.3 ± 7.4	119.4 ± 12.4	−0.08 ± 0.06	−0.02 ± 0.07	8.07 ± 1.84	≥0.20
12:31:28.52	+25:47:54.95	1249.9 ± 19.3	177.5 ± 17.8	−0.10 ± 0.05	−0.07 ± 0.10	–	–
12:31:21.17	+25:48:12.52	1259.0 ± 17.6	142.5 ± 16.2	−0.02 ± 0.03	−0.03 ± 0.08	–	–
12:31:24.64	+25:48:16.09	1263.7 ± 12.4	112.3 ± 15.9	−0.07 ± 0.04	−0.03 ± 0.04	–	–
12:31:23.55	+25:48:37.64	1287.4 ± 20.8	102.7 ± 25.1	−0.04 ± 0.03	0.03 ± 0.03	–	–
12:31:20.66	+25:48:43.54	1246.3 ± 35.4	150.1 ± 32.6	−0.02 ± 0.04	−0.05 ± 0.03	–	–
12:31:20.13	+25:44:54.37	1328.2 ± 25.9	126.1 ± 27.8	−0.05 ± 0.03	−0.01 ± 0.03	–	–
12:31:24.20	+25:44:55.43	1382.9 ± 24.8	118.9 ± 24.4	−0.02 ± 0.04	0.00 ± 0.04	–	–
12:31:23.67	+25:45:14.29	1383.1 ± 13.9	107.3 ± 19.2	0.02 ± 0.05	0.04 ± 0.05	4.49 ± 3.67	−1.54 ± 1.50
12:31:17.77	+25:45:25.17	1318.6 ± 32.2	81.4 ± 36.8	0.00 ± 0.02	−0.01 ± 0.02	–	–
12:31:22.24	+25:45:28.30	1406.2 ± 10.0	100.1 ± 16.3	0.00 ± 0.04	0.05 ± 0.04	5.99 ± 2.97	−0.39 ± 4.59
12:31:24.82	+25:45:31.82	1386.6 ± 8.9	111.2 ± 15.4	−0.05 ± 0.04	0.03 ± 0.05	5.12 ± 2.31	−1.28 ± 0.94
12:31:23.86	+25:45:55.41	1409.0 ± 6.0	108.3 ± 9.3	−0.04 ± 0.02	0.03 ± 0.04	5.64 ± 0.84	−0.82 ± 0.73
12:31:23.88	+25:46:01.66	1399.7 ± 5.7	130.1 ± 9.0	−0.06 ± 0.01	0.03 ± 0.09	5.92 ± 0.44	−0.51 ± 0.68
12:31:21.61	+25:46:06.63	1369.3 ± 6.5	126.0 ± 9.9	0.00 ± 0.02	0.03 ± 0.03	6.05 ± 1.31	−0.18 ± 4.85

Table A1 – *continued*

α (hh:mm:ss) (1)	δ (dd:mm:ss) (2)	V_{obs} (km s^{-1}) (3)	σ (km s^{-1}) (4)	h_3 (5)	h_4 (6)	CaT_{F09} (Å) (7)	[Fe/H] (dex) (8)
12:31:20.08	+25:46:07.64	1334.7 ± 9.6	110.9 ± 10.5	−0.07 ± 0.04	−0.06 ± 0.04	–	–
12:31:19.91	+25:46:20.47	1345.6 ± 10.3	71.1 ± 12.2	−0.04 ± 0.05	−0.01 ± 0.05	5.23 ± 2.55	−1.18 ± 2.22
12:31:22.65	+25:46:25.04	1358.3 ± 5.4	138.6 ± 8.5	0.00 ± 0.01	−0.02 ± 0.02	5.83 ± 0.27	−0.65 ± 0.42
12:31:23.46	+25:46:47.38	1292.4 ± 5.4	141.7 ± 8.3	0.04 ± 0.01	0.01 ± 0.05	5.82 ± 0.31	−0.66 ± 0.48
12:31:22.11	+25:46:59.87	1306.0 ± 6.0	114.4 ± 10.2	0.08 ± 0.02	0.03 ± 0.05	5.84 ± 0.86	−0.62 ± 1.32
12:31:21.88	+25:47:04.71	1304.2 ± 7.4	108.3 ± 9.7	0.03 ± 0.04	−0.10 ± 0.13	–	–
12:31:21.26	+25:47:19.61	1319.2 ± 8.7	109.4 ± 14.2	0.07 ± 0.04	−0.02 ± 0.07	5.30 ± 2.74	−1.12 ± 2.39
12:31:20.45	+25:47:23.12	1304.5 ± 9.7	106.2 ± 13.0	−0.07 ± 0.04	−0.11 ± 0.04	4.28 ± 3.54	−1.62 ± 1.45
12:31:17.92	+25:47:25.76	1312.0 ± 16.9	119.3 ± 21.5	−0.02 ± 0.04	0.00 ± 0.04	–	–
12:31:17.63	+25:47:38.50	1230.7 ± 28.7	143.0 ± 21.5	−0.07 ± 0.04	−0.01 ± 0.06	–	–
12:31:21.48	+25:47:59.50	1238.8 ± 18.8	148.0 ± 35.5	0.02 ± 0.04	−0.06 ± 0.05	–	–
12:31:19.02	+25:45:39.11	1348.3 ± 9.9	68.1 ± 30.9	0.07 ± 0.05	0.15 ± 0.08	–	–
12:31:31.43	+25:47:16.75	1393.5 ± 24.3	314.5 ± 47.8	0.04 ± 0.04	0.13 ± 0.09	–	–
12:31:23.50	+25:45:58.76	1391.5 ± 5.5	128.4 ± 8.7	0.00 ± 0.01	0.04 ± 0.02	6.19 ± 0.37	≥0.20
12:31:25.55	+25:46:13.94	1373.4 ± 5.4	135.5 ± 8.6	0.01 ± 0.01	−0.01 ± 0.02	5.97 ± 0.11	−0.42 ± 0.17
12:31:17.63	+25:47:38.50	1343.6 ± 12.0	48.4 ± 20.2	−0.06 ± 0.05	0.09 ± 0.06	–	–
12:31:19.58	+25:45:42.06	1344.9 ± 5.9	83.7 ± 16.0	0.07 ± 0.04	0.22 ± 0.11	–	–
12:31:16.75	+25:45:43.43	1418.9 ± 23.1	258.6 ± 56.3	0.04 ± 0.05	0.11 ± 0.11	–	–
12:31:19.49	+25:46:08.77	1356.1 ± 7.4	102.4 ± 13.2	0.08 ± 0.04	0.13 ± 0.09	5.45 ± 2.08	−0.99 ± 1.81
12:31:26.16	+25:46:12.21	1370.2 ± 5.7	134.1 ± 9.4	0.05 ± 0.02	0.04 ± 0.03	6.35 ± 0.29	≥0.20
12:31:19.06	+25:46:34.33	1339.8 ± 12.3	141.9 ± 19.6	0.09 ± 0.06	0.06 ± 0.06	5.91 ± 1.89	−0.51 ± 2.92
12:31:24.31	+25:46:35.54	1322.5 ± 5.1	150.6 ± 8.2	−0.02 ± 0.01	0.00 ± 0.02	6.23 ± 0.78	≥0.20
12:31:21.88	+25:47:04.71	1295.9 ± 5.4	122.0 ± 9.1	−0.04 ± 0.02	0.07 ± 0.09	6.33 ± 0.57	≥0.20
12:31:22.61	+25:47:06.37	1293.2 ± 5.4	114.0 ± 8.3	0.08 ± 0.02	0.07 ± 0.02	5.98 ± 0.59	−0.41 ± 0.92
12:31:29.23	+25:47:06.53	1341.8 ± 9.8	118.9 ± 25.8	0.16 ± 0.03	0.11 ± 0.05	–	–
12:31:25.62	+25:47:12.56	1297.0 ± 7.3	123.7 ± 11.6	0.05 ± 0.02	0.03 ± 0.03	6.48 ± 0.44	≥0.20
12:31:24.51	+25:47:13.74	1284.8 ± 5.7	118.8 ± 8.8	0.07 ± 0.02	0.01 ± 0.06	6.03 ± 0.63	−0.26 ± 2.34
12:31:30.42	+25:47:16.60	1324.1 ± 8.4	64.5 ± 24.4	−0.06 ± 0.04	0.07 ± 0.08	–	–
12:31:24.76	+25:47:19.86	1285.8 ± 5.7	123.7 ± 8.9	0.01 ± 0.03	−0.06 ± 0.08	6.33 ± 0.67	≥0.20
12:31:24.32	+25:48:04.68	1303.5 ± 8.4	131.9 ± 16.0	0.00 ± 0.04	0.04 ± 0.08	–	–
12:31:25.84	+25:48:08.14	1302.4 ± 9.8	126.0 ± 23.6	0.01 ± 0.04	0.00 ± 0.06	–	–
12:31:17.05	+25:48:09.49	1314.5 ± 18.2	142.5 ± 36.0	0.08 ± 0.05	0.05 ± 0.04	–	–
12:31:24.25	+25:48:28.77	1309.3 ± 12.3	67.7 ± 14.1	−0.18 ± 0.04	0.02 ± 0.11	–	–
12:31:24.17	+25:44:50.58	1391.3 ± 11.8	71.7 ± 20.7	0.08 ± 0.04	0.02 ± 0.06	–	–
12:31:25.76	+25:45:27.64	1400.5 ± 8.1	119.4 ± 13.0	−0.06 ± 0.04	0.03 ± 0.06	6.07 ± 1.41	−0.12 ± 5.20
12:31:21.12	+25:45:36.49	1381.9 ± 7.5	102.2 ± 12.3	0.01 ± 0.03	0.07 ± 0.04	6.64 ± 1.42	≥0.20
12:31:25.32	+25:45:37.61	1406.2 ± 6.4	94.0 ± 10.2	0.02 ± 0.03	0.04 ± 0.04	6.40 ± 0.92	≥0.20
12:31:19.58	+25:45:42.06	1367.6 ± 7.4	69.4 ± 15.0	0.04 ± 0.03	0.05 ± 0.05	–	–
12:31:20.78	+25:45:53.13	1369.5 ± 8.4	129.4 ± 10.0	−0.06 ± 0.03	−0.05 ± 0.03	6.37 ± 1.09	≥0.20
12:31:21.30	+25:47:22.68	1302.9 ± 7.9	144.1 ± 11.1	−0.02 ± 0.03	−0.04 ± 0.08	7.38 ± 0.39	≥0.20
12:31:24.51	+25:47:47.88	1304.5 ± 9.4	131.7 ± 12.9	−0.05 ± 0.04	−0.01 ± 0.06	7.72 ± 1.19	≥0.20
12:31:25.62	+25:47:12.56	1292.8 ± 5.9	118.3 ± 8.3	0.03 ± 0.02	0.02 ± 0.03	6.87 ± 0.39	≥0.20
12:31:23.86	+25:45:55.41	1406.7 ± 5.2	113.4 ± 8.4	−0.06 ± 0.01	0.05 ± 0.10	6.04 ± 0.39	−0.22 ± 1.43
12:31:19.50	+25:45:08.00	1384.8 ± 7.1	46.3 ± 10.0	0.01 ± 0.03	0.03 ± 0.04	–	–
12:31:21.03	+25:45:24.01	1369.1 ± 6.7	75.5 ± 10.2	0.10 ± 0.03	0.07 ± 0.03	–	–
12:31:27.32	+25:45:50.06	1368.8 ± 7.1	111.5 ± 11.7	0.01 ± 0.04	−0.02 ± 0.05	5.76 ± 1.32	−0.72 ± 1.15
12:31:27.19	+25:46:01.41	1369.5 ± 5.8	126.8 ± 9.3	−0.06 ± 0.02	0.02 ± 0.09	5.77 ± 0.86	−0.71 ± 0.75
12:31:17.50	+25:46:12.22	1341.6 ± 10.3	82.2 ± 11.0	0.05 ± 0.03	0.05 ± 0.04	–	–
12:31:22.26	+25:46:20.09	1366.4 ± 5.4	123.9 ± 8.5	−0.03 ± 0.01	0.06 ± 0.09	6.05 ± 0.29	−0.18 ± 1.06
12:31:14.73	+25:46:46.61	1360.7 ± 15.5	25.2 ± 23.9	−0.01 ± 0.03	−0.01 ± 0.02	–	–
12:31:25.22	+25:46:59.81	1293.4 ± 5.3	132.4 ± 8.2	0.01 ± 0.01	−0.01 ± 0.07	6.30 ± 0.17	≥0.20
12:31:29.62	+25:47:01.63	1362.9 ± 7.2	54.5 ± 13.4	0.04 ± 0.04	0.07 ± 0.03	–	–
12:31:19.56	+25:47:10.42	1319.9 ± 7.3	114.9 ± 12.0	−0.03 ± 0.04	−0.03 ± 0.05	6.42 ± 1.86	≥0.20
12:31:31.11	+25:47:14.87	1350.7 ± 7.2	31.7 ± 16.3	0.01 ± 0.02	0.00 ± 0.02	–	–
12:31:24.94	+25:47:27.47	1289.6 ± 6.0	124.7 ± 10.7	−0.04 ± 0.02	0.03 ± 0.08	6.73 ± 0.70	≥0.20
12:31:21.04	+25:47:38.77	1308.1 ± 7.9	111.6 ± 11.5	−0.06 ± 0.04	0.11 ± 0.12	8.12 ± 2.04	≥0.20
12:31:28.17	+25:47:45.65	1326.8 ± 10.8	128.4 ± 15.8	−0.05 ± 0.04	0.00 ± 0.06	–	–
12:31:23.57	+25:48:06.78	1279.2 ± 14.2	133.2 ± 18.5	−0.09 ± 0.04	−0.04 ± 0.04	–	–

Table A2. Individual spectroscopically confirmed GCs and UCDs around NGC 4494. Columns 2 and 3 give the position in right ascension and declination (J2000), respectively. Columns 4 to 10 present the photometry. The measured recession velocity is given in column 11, while values of the CaT_{F10} index and inferred [Fe/H], when available, are in columns 12 and 13, respectively. The errors on the quoted [Fe/H] are based on the index errors only and do not include systematics e.g. adopted calibration.

ID	α	δ	g_0	r_0	i_0	$(g-i)_0$	V_0	I_0	$(V-I)_0$	V_{obs}	CaT_{F10}	[Fe/H]
	(hh:mm:ss)	(dd:mm:ss)	(mag)	(mag)	(mag)	(mag)	(mag)	(mag)	(mag)	(km s^{-1})	(Å)	(dex)
(1)	(2)	(3)	(4)	(5)	(6)	(7)	(8)	(9)	(10)	(11)	(12)	(13)
						UCD						
UCD1	12:31:25.515	+25:46:19.77	20.17	19.45	19.11	1.06	–	–	–	1281 ± 5	7.64 ± 0.03	−0.30 ± 0.01
UCD2	12:31:24.643	+25:48:16.09	20.18	19.48	19.07	1.11	–	–	–	1341 ± 5	7.45 ± 0.01	−0.38 ± 0.01
UCD3	12:31:27.191	+25:46:01.41	20.32	19.66	19.28	1.04	–	–	–	1152 ± 5	7.59 ± 0.01	−0.32 ± 0.01
						GC						
GC1	12:31:17.633	+25:47:38.50	22.73	22.16	21.96	0.77	–	–	–	1215 ± 5	6.21 ± 0.50	−0.92 ± 0.22
GC1	12:31:17.633	+25:47:38.50	22.73	22.16	21.96	0.77	–	–	–	1198 ± 15	–	–
GC2	12:31:23.857	+25:45:55.41	21.25	20.56	20.23	1.01	–	–	–	1502 ± 5	6.69 ± 0.11	−0.71 ± 0.05
GC2	12:31:23.857	+25:45:55.41	21.25	20.56	20.23	1.01	–	–	–	1506 ± 6	8.10 ± 0.15	−0.09 ± 0.07
GC3	12:31:25.554	+25:46:13.94	21.48	20.88	20.56	0.92	–	–	–	1513 ± 7	6.22 ± 0.28	−0.92 ± 0.12
GC3	12:31:25.554	+25:46:13.94	21.48	20.88	20.56	0.92	–	–	–	1515 ± 13	5.80 ± 0.33	−1.10 ± 0.14
GC4	12:31:23.497	+25:45:58.76	21.46	20.78	20.32	1.14	–	–	–	1326 ± 5	8.74 ± 0.19	0.19 ± 0.08
GC4	12:31:23.497	+25:45:58.76	21.46	20.78	20.32	1.14	–	–	–	1327 ± 7	8.47 ± 0.25	0.07 ± 0.11
GC5	12:31:10.758	+25:44:39.03	22.28	21.84	21.59	0.69	–	–	–	1314 ± 10	4.21 ± 0.34	−1.80 ± 0.15
GC5	12:31:10.758	+25:44:39.03	22.28	21.84	21.59	0.69	–	–	–	1316 ± 14	4.21 ± 0.26	−1.80 ± 0.12
GC6	12:31:24.047	+25:46:48.18	20.71	19.99	19.61	1.10	20.82	19.72	1.10	1263 ± 5	8.46 ± 0.19	0.06 ± 0.08
GC7	12:31:23.382	+25:46:51.76	21.92	21.38	20.97	0.95	23.01	22.02	0.99	1328 ± 14	–	–
GC8	12:31:22.650	+25:46:25.04	21.58	20.97	20.60	0.98	–	–	–	1380 ± 7	–	–
GC9	12:31:25.641	+25:46:30.60	21.17	20.55	20.17	1.00	–	–	–	1496 ± 5	7.33 ± 0.22	−0.43 ± 0.10
GC10	12:31:24.152	+25:47:00.18	22.28	21.72	21.26	1.02	23.09	22.08	1.01	1363 ± 12	–	–
GC11	12:31:25.936	+25:46:46.71	20.85	20.23	19.97	0.88	–	–	–	1368 ± 5	6.08 ± 0.10	−0.98 ± 0.04
GC12	12:31:24.317	+25:47:10.83	21.13	20.60	20.29	0.84	20.90	20.00	0.90	1139 ± 5	–	–
GC13	12:31:21.611	+25:46:06.63	22.96	22.44	22.12	0.84	–	–	–	1160 ± 10	–	–
GC14	12:31:24.816	+25:45:31.82	23.17	22.56	22.10	1.07	–	–	–	1311 ± 9	–	–
GC15	12:31:26.061	+25:47:23.55	22.79	22.04	21.66	1.13	22.30	21.23	1.07	1292 ± 5	6.94 ± 0.48	−0.60 ± 0.21
GC16	12:31:19.909	+25:46:20.47	22.10	21.45	21.16	0.94	21.73	20.77	0.96	1468 ± 5	7.41 ± 0.20	−0.40 ± 0.09
GC17	12:31:20.083	+25:46:07.64	23.00	22.35	21.94	1.06	22.59	21.50	1.09	1378 ± 5	8.15 ± 0.51	−0.07 ± 0.22
GC18	12:31:27.864	+25:46:02.64	21.64	21.04	20.72	0.92	–	–	–	1253 ± 5	6.32 ± 0.14	−0.87 ± 0.06
GC19	12:31:21.259	+25:47:19.61	23.46	22.85	22.55	0.91	23.05	22.14	0.91	1114 ± 9	–	–
GC20	12:31:19.666	+25:47:06.41	21.27	20.75	20.49	0.78	20.96	20.15	0.81	1398 ± 5	4.18 ± 0.10	−1.81 ± 0.04
GC21	12:31:21.294	+25:47:32.93	21.70	21.19	20.92	0.78	21.40	20.59	0.81	1262 ± 5	4.56 ± 0.22	−1.64 ± 0.10
GC22	12:31:29.018	+25:46:50.84	22.54	21.85	21.45	1.08	–	–	–	1323 ± 5	8.08 ± 0.32	−0.10 ± 0.14
GC23	12:31:28.673	+25:45:50.66	23.61	22.95	22.56	1.05	–	–	–	1424 ± 15	–	–
GC24	12:31:19.459	+25:47:12.51	22.76	22.25	21.99	0.77	22.42	21.57	0.85	1235 ± 7	–	–
GC25	12:31:29.115	+25:45:58.29	22.62	21.92	21.53	1.09	–	–	–	1269 ± 5	7.20 ± 0.34	−0.49 ± 0.15
GC26	12:31:26.776	+25:45:18.12	23.12	22.63	22.41	0.70	–	–	–	1331 ± 11	–	–
GC27	12:31:28.524	+25:45:36.16	23.27	22.72	22.40	0.87	–	–	–	1334 ± 15	–	–
GC28	12:31:29.491	+25:45:59.14	22.19	21.65	21.40	0.80	–	–	–	1366 ± 5	–	–
GC29	12:31:30.262	+25:46:18.45	22.70	22.20	21.98	0.73	–	–	–	1301 ± 6	–	–
GC30	12:31:24.200	+25:44:55.43	23.24	22.61	22.30	0.94	–	–	–	1356 ± 7	–	–
GC31	12:31:20.711	+25:45:07.73	22.33	21.75	21.48	0.85	–	–	–	1338 ± 7	6.37 ± 0.30	−0.85 ± 0.13
GC32	12:31:21.476	+25:47:59.50	23.45	22.73	22.34	1.11	22.95	21.87	1.08	1319 ± 6	–	–
GC33	12:31:30.764	+25:46:32.54	22.36	21.88	21.61	0.76	–	–	–	1332 ± 7	–	–
GC34	12:31:17.921	+25:47:25.76	22.62	21.91	21.56	1.05	22.20	21.14	1.06	1319 ± 5	6.95 ± 0.28	−0.60 ± 0.12
GC35	12:31:28.516	+25:47:54.95	21.10	20.45	20.10	1.00	–	–	–	1341 ± 5	6.91 ± 0.07	−0.61 ± 0.03
GC36	12:31:29.854	+25:45:25.62	23.09	22.62	22.33	0.76	–	–	–	1435 ± 12	–	–
GC37	12:31:21.166	+25:48:12.52	23.32	22.77	22.47	0.85	22.92	22.13	0.79	1345 ± 7	–	–
GC38	12:31:26.805	+25:44:44.90	22.20	21.64	21.35	0.85	–	–	–	1263 ± 5	6.31 ± 0.23	−0.88 ± 0.10
GC39	12:31:17.769	+25:45:25.17	23.05	22.55	22.34	0.71	–	–	–	1360 ± 7	–	–
GC40	12:31:25.462	+25:44:26.26	22.99	22.40	22.14	0.86	–	–	–	1465 ± 7	–	–
GC41	12:31:31.954	+25:45:28.89	22.27	21.59	21.19	1.08	–	–	–	1224 ± 5	7.72 ± 0.19	−0.26 ± 0.08
GC42	12:31:28.335	+25:44:28.71	23.31	22.63	22.27	1.04	–	–	–	1533 ± 8	–	–
GC43	12:31:28.327	+25:48:33.16	23.33	22.69	22.36	0.97	–	–	–	1438 ± 6	–	–
GC44	12:31:23.196	+25:44:10.31	23.26	22.63	22.32	0.94	–	–	–	1467 ± 9	–	–
GC45	12:31:20.664	+25:48:43.54	20.54	19.94	19.63	0.91	20.29	19.37	0.92	1320 ± 5	6.41 ± 0.02	−0.83 ± 0.01
GC46	12:31:18.649	+25:44:25.92	21.71	21.22	20.98	0.72	–	–	–	1341 ± 5	3.64 ± 0.15	−2.04 ± 0.07
GC47	12:31:14.158	+25:46:05.08	22.92	22.34	22.03	0.89	–	–	–	1553 ± 6	–	–

Table A2 – *continued*

ID	α	δ	g_0	r_0	i_0	$(g-i)_0$	V_0	I_0	$(V-I)_0$	$V_{\rm obs}$	$\mathrm{CaT_{F10}}$	[Fe/H]
	(hh:mm:ss)	(dd:mm:ss)	(mag)	(mag)	(mag)	(mag)	(mag)	(mag)	(mag)	(km s^{-1})	(Å)	(dex)
(1)	(2)	(3)	(4)	(5)	(6)	(7)	(8)	(9)	(10)	(11)	(12)	(13)
GC48	12:31:22.893	+25:49:02.68	22.48	21.82	21.50	0.98	22.13	21.16	0.97	1271 ± 5	5.21 ± 0.33	−1.36 ± 0.15
GC49	12:31:25.473	+25:43:42.88	22.23	21.63	21.35	0.88	–	–	–	1398 ± 5	6.26 ± 0.20	−0.90 ± 0.09
GC50	12:31:14.214	+25:47:54.84	22.23	21.67	21.40	0.83	–	–	–	1540 ± 5	–	–
GC51	12:31:19.664	+25:43:45.66	21.67	21.09	20.83	0.84	–	–	–	1387 ± 5	6.36 ± 0.11	−0.86 ± 0.05
GC52	12:31:32.477	+25:48:42.98	23.86	23.23	22.80	1.06	–	–	–	1320 ± 13	–	–
GC53	12:31:16.502	+25:44:04.40	23.42	22.83	22.56	0.85	–	–	–	1335 ± 11	–	–
GC54	12:31:28.085	+25:49:28.15	23.17	22.52	22.22	0.95	–	–	–	1315 ± 14	–	–
GC55	12:31:27.746	+25:43:27.59	23.36	22.81	22.49	0.87	–	–	–	1391 ± 9	–	–
GC56	12:31:33.979	+25:44:30.97	23.22	22.54	22.15	1.07	–	–	–	1545 ± 10	–	–
GC57	12:31:19.620	+25:43:28.65	21.26	20.70	20.43	0.83	–	–	–	1524 ± 5	6.41 ± 0.06	−0.83 ± 0.03
GC58	12:31:26.154	+25:49:46.51	23.27	22.61	22.28	0.98	22.92	21.94	0.98	1260 ± 5	–	–
GC59	12:31:18.674	+25:49:36.02	23.51	22.82	22.48	1.03	23.14	22.19	0.95	1155 ± 13	–	–
GC60	12:31:10.815	+25:44:31.70	23.28	22.70	22.38	0.90	–	–	–	1371 ± 7	–	–
GC61	12:31:15.751	+25:49:59.03	22.17	21.61	21.34	0.83	–	–	–	1316 ± 5	4.88 ± 0.25	−1.50 ± 0.11
GC62	12:31:28.879	+25:42:37.80	22.68	22.22	21.99	0.69	–	–	–	1423 ± 8	–	–
GC63	12:31:17.817	+25:50:15.03	23.48	22.98	22.74	0.74	–	–	–	1160 ± 12	–	–
GC64	12:31:21.059	+25:50:55.11	22.63	22.09	21.84	0.79	–	–	–	1192 ± 7	6.22 ± 0.46	−0.92 ± 0.20
GC65	12:31:19.514	+25:51:23.09	22.76	22.23	21.97	0.79	–	–	–	1208 ± 8	–	–
GC66	12:31:19.514	+25:51:23.09	22.76	22.23	21.97	0.79	–	–	–	1183 ± 11	–	–
GC67	12:31:23.204	+25:41:24.27	22.71	22.17	21.92	0.79	–	–	–	1414 ± 5	6.28 ± 0.41	−0.89 ± 0.18
GC68	12:31:09.929	+25:42:25.62	23.33	22.73	22.39	0.94	–	–	–	1388 ± 10	–	–
GC69	12:31:12.260	+25:51:02.36	21.72	21.10	20.82	0.90	–	–	–	1427 ± 5	6.23 ± 0.13	−0.91 ± 0.06
GC70	12:31:24.963	+25:41:05.03	22.66	22.19	21.95	0.71	–	–	–	1409 ± 11	5.55 ± 0.46	−1.21 ± 0.20
GC71	12:31:45.488	+25:45:07.86	23.54	22.89	22.61	0.93	–	–	–	1198 ± 9	–	–
GC72	12:31:31.665	+25:41:00.70	20.98	20.41	20.07	0.92	–	–	–	1280 ± 12	6.64 ± 0.05	−0.73 ± 0.02
GC73	12:31:12.603	+25:41:11.20	23.67	23.14	22.83	0.84	–	–	–	1386 ± 13	–	–
GC74	12:31:14.644	+25:53:55.85	22.49	21.86	21.55	0.94	–	–	–	1413 ± 10	5.07 ± 0.35	−1.42 ± 0.15
GC75	12:31:28.327	+25:48:33.16	23.33	22.69	22.36	0.97	–	–	–	1434 ± 18	–	–
GC76	12:31:19.576	+25:45:42.06	22.55	22.09	21.83	0.72	22.28	21.50	0.78	1326 ± 22	–	–
GC77	12:31:16.751	+25:45:43.43	22.96	22.41	22.17	0.79	–	–	–	1353 ± 16	–	–
GC78	12:31:19.486	+25:46:08.77	21.25	20.71	20.41	0.84	20.95	20.01	0.94	1481 ± 5	6.36 ± 0.09	−0.86 ± 0.04
GC79	12:31:26.160	+25:46:12.21	21.40	20.81	20.50	0.90	–	–	–	1576 ± 10	–	–
GC80	12:31:19.059	+25:46:34.33	23.47	22.93	22.72	0.75	23.10	22.23	0.87	1315 ± 34	–	–
GC81	12:31:04.423	+25:46:42.43	22.41	21.85	21.58	0.83	–	–	–	1370 ± 14	6.64 ± 0.32	−0.73 ± 0.14
GC82	12:31:22.609	+25:47:06.37	22.25	21.61	21.21	1.05	21.98	20.91	1.07	1249 ± 8	6.88 ± 0.32	−0.63 ± 0.14
GC83	12:31:29.233	+25:47:06.53	22.85	22.26	21.95	0.90	–	–	–	1331 ± 17	–	–
GC84	12:31:24.760	+25:47:19.86	23.40	22.75	22.44	0.95	23.16	22.04	1.12	1264 ± 18	–	–
GC85	12:31:14.916	+25:47:22.94	22.97	22.38	22.15	0.82	–	–	–	1184 ± 10	–	–
GC86	12:31:25.845	+25:48:08.14	22.63	22.04	21.75	0.88	–	–	–	1237 ± 9	5.77 ± 0.40	−1.11 ± 0.18
GC87	12:31:30.852	+25:48:30.66	22.79	22.25	21.97	0.82	–	–	–	1302 ± 18	–	–
GC88	12:31:38.933	+25:52:23.84	21.63	20.94	20.62	1.02	–	–	–	1291 ± 8	6.12 ± 0.13	−0.96 ± 0.06
GC89	12:31:19.576	+25:45:42.06	22.55	22.09	21.83	0.72	22.28	21.50	0.78	1328 ± 13	3.56 ± 0.43	−2.08 ± 0.19
GC90	12:31:34.027	+25:48:57.55	23.49	22.89	22.58	0.91	–	–	–	1394 ± 13	–	–
GC91	12:31:19.514	+25:51:23.09	22.76	22.23	21.97	0.79	–	–	–	1192 ± 17	4.63 ± 0.40	−1.61 ± 0.18
GC92	12:31:16.396	+25:43:48.03	22.76	22.27	22.04	0.73	–	–	–	1438 ± 13	4.47 ± 0.37	−1.68 ± 0.16
GC93	12:31:15.042	+25:44:30.69	23.56	23.05	22.80	0.76	–	–	–	1391 ± 83	–	–
GC94	12:31:16.290	+25:44:33.65	23.07	22.56	22.30	0.78	–	–	–	1319 ± 55	–	–
GC95	12:31:19.503	+25:45:08.00	22.67	21.99	21.61	1.06	–	–	–	1478 ± 7	6.87 ± 0.27	−0.63 ± 0.12
GC96	12:31:17.292	+25:45:18.42	23.54	23.00	22.73	0.81	–	–	–	1397 ± 29	–	–
GC97	12:31:21.032	+25:45:24.01	23.36	22.72	22.37	0.98	22.96	21.93	1.03	1250 ± 15	–	–
GC98	12:31:27.323	+25:45:50.06	22.26	21.60	21.24	1.02	–	–	–	1246 ± 8	6.30 ± 0.23	−0.88 ± 0.10
GC99	12:31:22.262	+25:46:20.09	21.41	20.85	20.52	0.89	21.29	20.47	0.82	1450 ± 11	4.41 ± 0.11	−1.71 ± 0.05
GC100	12:31:14.730	+25:46:46.61	21.96	21.34	21.04	0.93	–	–	–	1337 ± 7	7.14 ± 0.15	−0.51 ± 0.07
GC101	12:31:25.222	+25:46:59.81	21.79	21.15	20.81	0.98	21.70	20.71	0.99	1355 ± 8	6.91 ± 0.33	−0.61 ± 0.14
GC102	12:31:29.616	+25:47:01.63	22.87	22.20	21.84	1.04	–	–	–	1417 ± 14	9.73 ± 0.38	0.62 ± 0.17
GC103	12:31:19.559	+25:47:10.42	22.39	21.70	21.32	1.08	21.92	20.87	1.05	1385 ± 7	7.60 ± 0.19	−0.31 ± 0.08
GC104	12:31:31.111	+25:47:14.87	22.34	21.67	21.28	1.06	–	–	–	1295 ± 8	8.15 ± 0.20	−0.07 ± 0.09
GC105	12:31:24.945	+25:47:27.47	22.64	21.89	21.52	1.12	22.19	21.10	1.09	1356 ± 8	8.10 ± 0.33	−0.10 ± 0.14
GC106	12:31:21.041	+25:47:38.77	22.40	21.78	21.55	0.85	22.08	21.19	0.89	1281 ± 9	6.23 ± 0.31	−0.91 ± 0.14
GC107	12:31:23.572	+25:48:06.78	22.25	21.75	21.48	0.76	–	–	–	1305 ± 9	5.88 ± 0.31	−1.07 ± 0.13
GC108	12:31:23.998	+25:49:03.53	23.87	23.33	23.09	0.78	23.50	22.67	0.83	1188 ± 13	–	–
GC109	12:31:38.597	+25:52:54.57	21.55	21.00	20.78	0.78	–	–	–	1361 ± 10	3.97 ± 0.11	−1.90 ± 0.05

by V03 or that the CaT behaves non-linearly with colour. In fact, the relationship between $(g-i)_0$ colours and CaT_{F10} is consistent with being linear, albeit with large observational scatter. This suggests that the strange distribution of CaT_{F10} values in the GCs around NGC 1407 may be best explained by the presence of hot blue stars in a significant number of its GCs after all.

APPENDIX C: NUMERICAL SIMULATIONS OF THE GC SYSTEM

In this section, we discuss whether the observed kinematics of blue and red GCs around NGC 4494 can be reproduced reasonably well via major merging between two disc galaxies with pre-existing blue and red GCs.

C1 Model description

In the following, we ignore the presence of the non-rotating intermediate colour GCs. We run *dissipationless* simulations (i.e. no gas dynamics and no new formation of stars and clusters) and compare the physical properties of the GC systems in the merger remnants to search for the model that best reproduces the following observed properties of blue and red GCs.

(i) The maximum rotational velocity ($V_{\rm rot,max}$) is as large as 100 km s^{-1} for blue GCs.
(ii) The central (maximum) velocity dispersion (σ) is as large as 150 km s^{-1} for both subpopulations.
(iii) $V_{\rm rot,max}/\sigma$ is larger than 0.3 for both metal-poor and metal-rich GCs.
(iv) $V_{\rm rot,max}$ is larger in the blue than in red GCs.

We consider that the latest (iv) is one of the key physical characteristics of the GCs around NGC 4494.

Since the numerical methods and techniques we employ for modelling the dynamical evolution of dissipationless mergers between two discs with GCs have been detailed elsewhere (Bekki et al. 2005; Bekki 2010), we give only a brief review focusing on the main particularities of this project here. The progenitor disc galaxies taking part in the merger are given a dark matter halo, bulge, thin exponential disc, as well as GCs initially located in the bulge (hereafter BGCs) and in the halo (HGCs). The total mass and size of the exponential disc (bulge) are $M_{\rm d}$ ($M_{\rm b}$) and $R_{\rm d}$ ($R_{\rm b}$), respectively. We show results from models where the progenitor disc galaxies are similar to the Galaxy (i.e. $M_{\rm b}=0.167M_{\rm d}$ and $R_{\rm b}=0.2R_{\rm d}$). In this work, the total (virial) mass of the dark matter halo ($M_{\rm dm}$) in a disc galaxy is set to be $9M_{\rm d}$.

The initial distribution of HGCs in the progenitor disc galaxies follows a power-law profile with index $\alpha=-3.5$. The extent of the HGC system ($R_{\rm HGC}$) is assumed to be $3R_{\rm d}$. In other words, the power-law distribution is truncated at $R=3R_{\rm d}$. The half-number radius of the HGC system is set to be $0.29R_{\rm d}$. The initial distribution of BGCs also follows the same power law but has a truncation radius of $r_{\rm gc}R_{\rm HGC}$, where $r_{\rm gc}$ controls the compactness of the spatial distribution of BGCs. We find that $r_{\rm gc}$ is important for determining the kinematical differences between HGCs and BGCs in the merger remnants.

In the present models, the inner metal-rich BGCs and outer metal-poor HGCs ultimately become blue and red GCs in NGC 4494, respectively. This is a simplification since additional metal-rich GCs may form from gas dynamics during galaxy merging (e.g. Bekki et al. 2002). Even so, the models may enable us to understand how large amounts of rotation are present in metal-poor and possibly metal-rich GCs around NGC 4494. For convenience, $V_{\rm rot,max}$ (σ) of HGCs (blue GCs) and BGCs (red GCs) are referred to as $V_{\rm rot,max,blue}$ ($\sigma_{\rm blue}$) and $V_{\rm rot,max,red}$ ($\sigma_{\rm red}$), respectively. Here $R_{\rm d}$ and $M_{\rm d}$ are set to be 13.4 kpc and $4.3\times10^{10}{\rm M}_{\odot}$, respectively, to reproduce the observed kinematics of the stars in NGC 4494.

The mass ratio of the two progenitor discs in the simulated mergers is 1 (i.e. equal-mass major merger) and the orbit of the two discs is initially set to be in the *xy*-plane for all models. The pericentre distance ($r_{\rm p}$) and the eccentricity ($e_{\rm p}$) of the merger are free parameters that influence the orbital energy and angular momentum. The spin of each progenitor galaxy is specified by two angles θ_i and ϕ_i. θ_i is the angle between the *z*-axis and the angular momentum vector of the $i^{\rm th}$ progenitor disc. ϕ_i is the azimuthal angle measured from the *x*-axis to the projection of the angular momentum vector of the $i^{\rm th}$ progenitor disc on to the *xy*-plane.

We mainly show the results for our 'fiducial model', which has $r_{\rm p}=2R_{\rm d}$, $e_{\rm p}=0.72$, $\theta_1=210^\circ$, $\theta_2=225^\circ$, $\phi_1=45^\circ$ and $\phi_2=120^\circ$, as it best reproduces the observed four key properties of the NGC 4494 GCs listed above. The fiducial model has an orbital configuration similar to 'retrograde-retrograde' merging (i.e. the orbital spin axis of the merger is anti-parallel to the intrinsic spin axes of the two discs). We also show the results of the models with 'prograde–prograde' ('prograde–retrograde') orbital configurations in which $\theta_1=30^\circ$ and $\theta_2=45^\circ$ ($\theta_1=30^\circ$ and $\theta_2=225^\circ$) and all other parameters unchanged. Model parameters and some salient results are given in Table C1.

When estimating the kinematics of the GC system and binned major-axis profiles, the merger remnant is assumed to be viewed

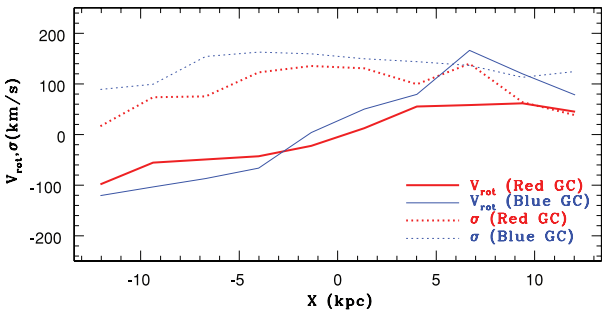

Figure C1. Line-of-sight rotational velocities ($V_{\rm rot}$, solid lines) and velocity dispersion (σ, dotted lines) for blue and red GCs along the *x*-axis in the merger remnant for the fiducial model (Model 1). Here the *y*-components of GC velocities are used for deriving the line of sight $V_{\rm rot}$ and σ at each bin along the *x*-axis. This figure is available in colour in the online version.

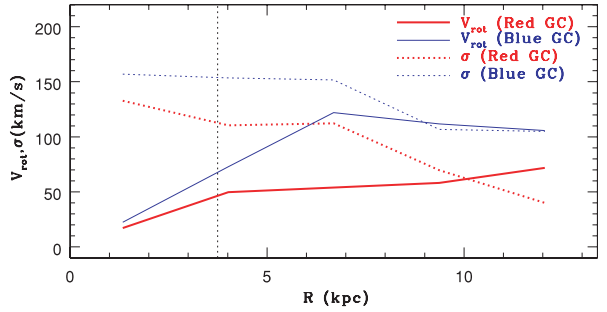

Figure C2. Same as Fig. C1 for the radial dependence directly comparable with the observational results in this work. The vertical dotted line indicates the effective radius of NGC 4494. This figure is available in colour in the online version.

Table C1. Model (column 1) parameter values and brief summary of results. Column 2 lists the pericentre distance of the merger in units of the disc size R_d. The orbital eccentricity of the merger is shown in column 3. Description of the orbits in column 4 is coded as follows: 'PP', 'PR' and 'RR' for prograde–prograde, prograde–retrograde and retrograde–retrograde merging, respectively. Columns 5 and 6 show the maximum rotational velocity of metal-poor and metal-rich GCs around the remnant, respectively. Columns 7 and 8 list the ratio of the maximum rotational velocity to the central velocity dispersion for metal-poor and metal-rich GCs, respectively.

Model	r_p ($\times R_d$)	e_p	Orbit	$V_{rot,max,blue}$ (km s^{-1})	$V_{rot,max,red}$ (km s^{-1})	$V_{rot,max,blue}/\sigma_{blue}$	$V_{rot,max,red}/\sigma_{red}$
(1)	(2)	(3)	(4)	(5)	(6)	(7)	(8)
1	2.0	0.72	RR	122	72	0.78	0.54
2	1.0	1.0	PP	47	75	0.35	0.66
3	2.0	1.0	PP	66	79	0.38	0.54
4	2.0	0.72	PP	81	111	0.57	0.86
5	2.0	0.72	PR	73	85	0.46	0.79

near to edge-on. In order to have enough objects in each bin, GCs at corresponding minor axis distances are included.

C2 Results

Fig. C1 shows the rotational velocity (V_{rot}) and velocity dispersion (σ) along the x-axis of the merger remnant for the fiducial model. The y-component of GC velocities for each of 10 bins is used for deriving line-of-sight profiles. Fig. C1 reveals that both metal-poor and metal-rich GCs exhibit global rotation ($-12 \leq x \leq 12$ kpc) albeit with stochastic scatter due to the small number of GCs in each bin. In fact, the apparently rapid change in V_{rot} around $x = 7$ kpc is due largely to small number statistics.

In order to compare the simulated profiles with the observed one, we investigate radial (R) profiles of the rotational velocity and velocity dispersion (Fig. C2). In the fiducial model, the larger amount of orbital angular momentum ($e_p = 0.72$ and $r_p = 2R_d$) allows the outer components (dark matter halo and HGCs) to acquire a large amount of rotation due to the efficient conversion of orbital angular momentum into spin angular momentum. For $R > R_e$ (=3.75 kpc), the simulated $V_{rot,blue}$ can be larger than 50 km s^{-1} (see Fig. C2) in agreement with the observations presented herein.

As shown in Table C1, the models with parabolic encounters (i.e. models 2 and 3) that initially have a significantly smaller amount of orbital angular momentum do not show large $V_{rot,max,blue}$ compared to the fiducial model. This implies that the observed large rotational velocity ($V_{rot}/\sigma \sim 0.7$) may help constrain the orbits of the progenitors of NGC 4494. Moreover, the small e_p in the fiducial model suggests that the progenitor galaxies were either a binary pair of galaxies or two large galaxies dominating a small bound group.

Fig. C2 also shows that even though the red GCs (BGCs) do have rotation, their rotational amplitude is smaller than that of the blue GCs. In the present models, the final kinematics of red GCs may become comparable to those of the stellar components of the merger remnants as a result of the adopted $r_{gc} = 0.1$. The fiducial model has a retrograde–retrograde orbital configuration yielding a final stellar remnant with apparently low rotation (<50 km s^{-1}) depending on the viewing angle. Fig. C2 shows that $V_{rot,max,red}$ is significantly smaller than $V_{rot,max,blue}$ as observed in NGC 4494. Moreover, as shown in Table C1, models with prograde–prograde and prograde–retrograde orbital configurations do not yield large kinematic differences between blue and red GCs. This suggests that the orbital configuration of disc–disc major mergers may be the key factor in causing the observed kinematic differences between blue and red GCs.

We thus conclude that the observed kinematics of the GC system around NGC 4494 are *broadly* consistent with a formation scenario wherein the remnant galaxy formed via major disc–disc merging, involved large amounts of orbital angular momentum and an initial retrograde–retrograde orbital configuration. An interesting prediction of the fiducial model is that the dark matter halo of NGC 4494 also has a significant amount of global rotation. The predicted maximum line-of-sight rotational velocity of the dark matter halo is ~40 km s^{-1} and $V_{rot}/\sigma \sim 0.25$. However, the simulated rotation profile of the red GCs (~50 km s^{-1}) is larger than the observed one (~20 km s^{-1}) for $R \sim 1$–$2R_e$ (corresponding to 3.8–7.6 kpc). We do not find models that show comparably low remnant red GC rotation whenever the remnant rotation of the blue GCs is large ($V_{rot,max,blue} \sim$ 100 km s^{-1}). This could mean that physical processes other than the collisionless major merger scenario explored in this study may be necessary to explain all observed stellar and GC kinematics NGC 4494 in a fully self-consistent manner.

SUPPORTING INFORMATION

Additional Supporting Information may be found in the online version of this article:

Table 3. Catalogue of photometrically selected GC candidates with $i_0 < 24$.
Table 4. List of spectroscopically identified contaminants and non-GC fillers.

Please note: Wiley-Blackwell are not responsible for the content or functionality of any supporting materials supplied by the authors. Any queries (other than missing material) should be directed to the corresponding author for the article.

This paper has been typeset from a TEX/LATEX file prepared by the author.